ÉCOLE POLYTECHNIQUE – LABORATOIRE D'HYDRODYNAMIQUE

MASTER 2 MFFA
MÉCANIQUE DES FLUIDES, FONDEMENTS ET APPLICATIONS

RESEARCH INTERNSHIP

A GLOBAL MAP OF TIDAL DISSIPATION OVER ABYSSAL HILLS

ADRIEN LEFAUVE

SUPERVISOR:
CAROLINE MULLER

MARCH 10TH – SEPTEMBER 1ST, 2014

Abstract

Internal gravity waves are complex oscillations widely found in fluids exhibiting density stratification, such as the ocean. Such waves may be produced by tidal currents flowing over rough seafloors; they are then called *internal tides*. As they travel away from the seafloor, internal tides tend to attain high amplitudes and break into turbulent eddies. Their ability to carry and dissipate part of energy make them of utmost importance in physical oceanography. Their intensive study in the past decades revealed that the breaking of internal tides may provide a large part of the power needed to mix the deep ocean and sustain the deep part of the meridional overturning circulation. The fraction of energy that those waves locally dissipate and the resulting vertical mixing distribution are crucial data for the parametrization of oceanic models, yet they remain poorly quantified.

In this work, we provide the first estimate of the worldwide three-dimensional distribution of internal tide dissipation by means of large-scale numerical simulations. We couple linear wave theory with a simple nonlinear breaking scheme and use global topography, stratification and tidal current data to reproduce the generation, upward propagation and energy dissipation of internal tides. We show that exceptionally high dissipation is commonly attained at a few hotspots, confined above mid-ocean spreading ridges in the Southern Hemisphere. As expected by earlier studies, we find that a large part of the resulting mixing follows an exponential decay with height, with strong bottom intensities. We however show that substantial mixing over smoother flanks follows a so far unreported non-monotonic vertical profile with significant mid-depth maxima.

Based on the literature studying the impact of internal-tide-driven mixing, we try to connect our findings to potential implications for the global oceanic circulation, which are still to be confirmed. In this spirit, we also provide a simple analytical tool to estimate the most relevant parameters of our three-dimensional map based on the expected wave amplitudes at the bottom. We find that predicting the whole nonlinear dissipation profile from a single local measure of bottom instability is indeed possible. Thereby linked to seafloor properties, stratification and tidal forcing, the map should allow for time-evolving parametrizations in long-term climate simulations.

Acknowledgements

I would like to express my gratitude to Caroline Muller for giving me the opportunity to start working on this interesting topic in the framework of a Laboratory Research Project, a few months before the formal start of this research internship. Her constant guidance throughout our project has been of inestimable value. I am especially grateful for her help and patience during long research meetings which contributed to develop my interest in this topic. Her advice and insightful suggestions greatly contributed to the completion of this work.

I am also grateful to all of the people working in LadHyX: my class and office mates Charu Datt and Keshav Raja, with whom I shared more than a office; the PhD students Mathieu Blanchard, Eline Dehandschoewercker, Emmanuel Du Pontavice, Marine Guémas, Gaëtan Lerisson, Timothé Mouterde, Chakri Ravilla, Emmanuel Virot, Eunok Yim, and postdocs Jeremy Basley, Daniel Rodriguez, Onofrio Semeraro, Gordon Taub for sharing interesting discussions, lunches (and sometimes computer time!). My thanks also go the all the researchers in LadHyX, especially Paul Billant, Jean-Marc Chomaz, Sabine Ortiz for our interesting ”geophysics meetings” and to the technical staff, Daniel Guy and Toaï Vu for their precious assistance with computer issues.

All these people and all those I did not mention contributed to make the atmosphere in LadHyX − casual and studious at the same time − so particular and enjoyable. I thank all of them and owe them most of what I have learned during my time here.

Contents

Chapter 1

Introduction and objectives

Among the rich variety of topics that the field of geophysical fluid dynamics encompasses, the interaction of moving fluids of varying density with fixed obstacles has been and remains the subject of intense investigation. Such systems are known to exhibit so-called *internal gravity waves*, which are generated where the flow is deviated, and propagate with unfamiliar properties into the bulk of the fluid. On Earth, this phenomenon is ubiquitous and may be observed in the atmosphere (winds over mountains) or oceans (currents over undulating seafloors).

In the deep ocean, of great interest is the radiation of internal waves as a consequence of tidal currents oscillating over rough hills. During their propagation from the seafloor to the ocean surface, these waves called *internal tides* often experience turbulence, initiated by wave-wave or wave-flow interactions. A significant fraction of the energy that they extract from the tide may be lost in small-scale eddies above the seafloor, which efficiently mixes waters of different densities. This *diapycnal mixing* (mixing across density surfaces) has important consequences on the energy budget of the ocean and hence on its stratification and dynamics, impacting the global climate due to the intimate ocean-atmosphere coupling. In this context, this work aims at understanding and quantifying the distribution and intensity of this mixing by the study of internal tide dissipation. The phenomena we are concerned with occur at scales which defy the current capabilities of global climate models, hence their effect has to be parametrized. We therefore aim at providing worldwide predictions of the spatial and vertical distribution of the internal-tide-driven mixing.

Observations estimate that as much as 1 TW (1 TW = 10^{12} W) of tidal energy could be dissipated in the deep ocean [1], but where and how this energy dissipates is unclear. In situ measurements report enhanced diapycnal diffusivities of several orders of magnitude, from $O(10^{-5})$ to $O(10^{-2})$ m^2 s^{-1} above rough seafloors [2]. Strong evidence suggests that it is mainly sustained by the turbulent dissipation of internal tides generated by abyssal hills, which are small-scale topographic features produced by volcanic activity at oceanic spreading ridges. The generation and propagation of these waves received much scrutiny but less is known about their instability and breaking. In this work, we adopt a nonlinear saturation model which predicts wave breaking and the resulting energy dissipation profile with height. Our numerical model is applied to recent worldwide tidal and stratification data, and a precise statistical description of the seafloor. We introduce the main theoretical concepts in Chapter 2 and our methodology in Chapter 3. Our results are then presented and discussed in Chapter 4.

Chapter 2

Background: theoretical toolbox

The first Sections 2.1-2.4 review the linear theory of internal tide generation and propagation in the ocean, under the approximation of slowly varying stratification. Section 2.5 describes our model for nonlinear wave breaking and associated energy dissipation. Finally, Section 2.6 describes the statistical representation of the small-scale topography relevant for tidal dissipation.

2.1 Primitive equations

We start by recalling the equations of geophysical fluid dynamics under relevant approximations. In the next Section 2.2, we introduce the Boussinesq model and focus on the propagation of small perturbations. This brings us to the characterization of internal gravity waves.

We consider the inviscid flow of a fluid of velocity $\mathbf{u}(\mathbf{x},t)$ with components (u,v,w), total pressure $p(\mathbf{x},t)$, density $\rho(\mathbf{x},t)$ in the field of gravity $\mathbf{g}$. We describe this flow in a framework rotating at angular speed Ω, well suited for flows at the surface of the Earth (see Fig. 2.1). The continuity and momentum equations governing the fluid motion are respectively

$$\begin{aligned} \frac{D\rho}{Dt} + \rho\nabla\cdot\mathbf{u} &= 0, & (2.1\text{a}) \\ \frac{D\mathbf{u}}{Dt} + 2\Omega\times\mathbf{u} &= -\frac{1}{\rho}\nabla p - \nabla\Phi, & (2.1\text{b}) \end{aligned}$$

where $D/Dt = \partial/\partial t + \mathbf{u}\cdot\nabla$ denotes the material derivative and the geopotential Φ simply reduces to $-\nabla\Phi = \mathbf{g}$ neglecting centrifugal forces. We next introduce a widely used set of two consistent assumptions:

- the *shallow fluid approximation*, decomposing the radius of the position vector $r\mathbf{e_r}$ in $r = a + z$, where a is the radius of the Earth and $z \ll a$, and
- the *traditional approximation* neglecting Coriolis terms involving w in the horizontal momentum equations and metric terms in uw/r and vw/r.

To ensure energy conservation, and since we refuse to make the common *hydrostatic approximation* here, the Coriolis and metric terms in the vertical momentum balance must be cancelled as well [3]. Eq. (2.1b) then

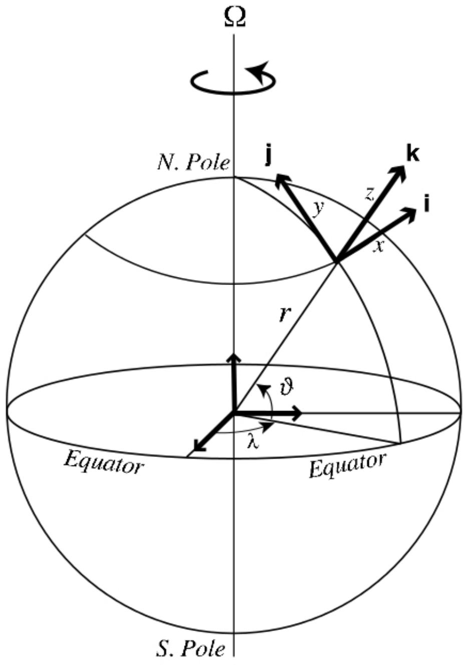

FIG. 2.1: Spherical coordinate system (r, λ, θ) and rotating frame of reference for geophysical flows inducing Coriolis forces. Note the tangent plane with local Cartesian coordinates (x, y, z). Reproduced from [3].

becomes

$$\begin{aligned}
\frac{Du}{Dt} - \left(2\Omega + \frac{u}{(a+\cancel{z})\cos\theta}\right)(v\sin\theta - \cancel{w\cos\theta}) &= -\frac{1}{\rho(a+\cancel{z})\cos\theta}\frac{\partial p}{\partial\lambda}, && (2.2a)\\
\frac{Dv}{Dt} + \cancel{\frac{vw}{a+z}} + \left(2\Omega + \frac{u}{(a+\cancel{z})\cos\theta}\right)u\sin\theta &= -\frac{1}{\rho(a+\cancel{z})}\frac{\partial p}{\partial\theta}, && (2.2b)\\
\frac{Dw}{Dt} - \cancel{\frac{u^2+v^2}{a+z} - 2\Omega u\cos\theta} &= -\frac{1}{\rho}\frac{\partial p}{\partial(\cancel{a}+z)} - g. && (2.2c)
\end{aligned}$$

with the convective derivative

$$\frac{D}{Dt} = \frac{\partial}{\partial t} + \frac{u}{(a+\cancel{z})\cos\theta}\frac{\partial}{\partial\lambda} + \frac{v}{a+\cancel{z}}\frac{\partial}{\partial\theta} + w\frac{\partial}{\partial(\cancel{a}+z)}. \tag{2.2d}$$

The following relations for our spherical coordinate system were used (see Fig. 2.1):

$$\frac{D\mathbf{u}}{Dt} = \frac{D}{Dt}\begin{pmatrix} u \\ v \\ w \end{pmatrix} + \underbrace{\begin{pmatrix} -v/r \\ u/r \\ u\tan\theta/r \end{pmatrix}}_{\Omega_{\text{flow}}} \times \begin{pmatrix} u \\ v \\ w \end{pmatrix}, \quad \frac{D}{Dt} = \frac{\partial}{\partial t} + \frac{u}{r\cos\theta}\frac{\partial}{\partial\lambda} + \frac{v}{r}\frac{\partial}{\partial\theta} + w\frac{\partial}{\partial r}, \quad \text{and} \quad \Omega = \begin{pmatrix} 0 \\ \Omega\cos\theta \\ \Omega\sin\theta \end{pmatrix}. \tag{2.3}$$

The horizontal momentum equations can take a simpler form if we slightly modify the material derivative of the unit vectors $\mathbf{i}$, $\mathbf{j}$ as follows:

$$\text{from} \quad \frac{D\mathbf{i}}{Dt} = \Omega_{\text{flow}} \times \mathbf{i} \qquad \text{to} \qquad \frac{\widetilde{D}\mathbf{i}}{\widetilde{D}t} = \widetilde{\Omega}_{\text{flow}} \times \mathbf{i} = \begin{pmatrix} 0 \\ 0 \\ u\tan\theta/r \end{pmatrix} \times \mathbf{i} = \frac{u\tan\theta}{a}\mathbf{j}, \tag{2.4a}$$

and similarly

$$\frac{\widetilde{D}\mathbf{j}}{\widetilde{D}t} = \widetilde{\Omega}_{\text{flow}} \times \mathbf{j} = -\frac{u\tan\theta}{a}\mathbf{i}, \tag{2.4b}$$

where $\widetilde{\Omega}_{\text{flow}}$ is the vertical component of Ω_{flow}. As a result, the accelerations $uv\tan\theta/a$ in Eq. (2.2a) and $u^2\tan\theta/a$ in in Eq. (2.2b) disappear and the primitive equations Eqs. (2.2) finally reduce to the compact vector equation

$$\frac{\widetilde{D}\mathbf{u}}{\widetilde{D}t} + \mathbf{f}\times\mathbf{u} = -\frac{1}{\rho}\nabla p + \mathbf{g}, \tag{2.5}$$

where $\nabla = [(a\cos\theta)^{-1}\partial/\partial\lambda, a^{-1}\partial/\partial\theta, \partial/\partial z]$ and $\mathbf{f} = 2\Omega\sin\theta\ \mathbf{k}$. This equation describes a system in which the rotation vector is aligned with the local vertical. In the following, we shall drop the $\widetilde{\ }$.

For the study phenomena at scales where the *sphericity* of the Earth is not important (but the rotation *is*), we can further simplify these equations by performing a local Cartesian approximation. We define an ad hoc *Cartesian tangent plane* at longitude λ_0 and latitude θ_0 in which $(x,y,z) = (a\cos\theta_0(\lambda-\lambda_0), a(\theta-\theta_0), z)$, so $(dx,dy,dz) = (a\cos\theta_0 d\lambda, ad\theta, dz)$. In this approach, (u,v,w) approximate the velocity in the tangent plane (respectively the East-West, North-South and vertical velocity), and Eq. (2.2) transforms to

$$\frac{Du}{Dt} - fv = -\frac{1}{\rho}\frac{\partial p}{\partial x}, \tag{2.6a}$$

$$\frac{Dv}{Dt} + fu = -\frac{1}{\rho}\frac{\partial p}{\partial y}, \tag{2.6b}$$

$$\frac{Dw}{Dt} = -\frac{1}{\rho}\frac{\partial p}{\partial z} - g. \tag{2.6c}$$

with $D/Dt = \partial/\partial t + u\partial/\partial x + v\partial/\partial y + w\partial/\partial z$ and $f = 2\Omega\sin\theta_0$ is the Coriolis parameter [$\Omega = 2\pi/(3600\times 24) \approx 7.3\times 10^{-5}\ \text{s}^{-1}$]. In the following, we shall use this so-called *f-plane approximation*. To complete our set of governing equations for the five variables u, v, w, ρ, p, we shall discuss the continuity equation and add an equation enforcing the conservation of energy.

2.2 Internal gravity waves

The next important approximation relies on the relatively small variations in density observed in most geophysical fluids, and especially in the ocean, where the combined effects of pressure compressibility, thermal and saline contraction remain very small [3]. We shall therefore adopt the *Boussinesq approximation*, which decomposes the density field into $\rho(\mathbf{x},\mathbf{t}) = \rho_0 + \bar{\rho}(z) + \rho'(\mathbf{x},\mathbf{t})$, where $\bar{\rho}, \rho' \ll \rho_0$, and $\bar{\rho}$ balances the gravitational acceleration [similarly, $p(\mathbf{x},\mathbf{t}) = \bar{p}(z) + p'(\mathbf{x},\mathbf{t})$]. The idea of this approximation is to retain the effect of variable density *only in the vertical acceleration term* ($\rho \approx \rho_0$ is assumed in the horizontal momentum equations). The buoyancy force in the vertical momentum equation then takes the form

$$b = -\frac{g\rho'}{\rho_0}. \tag{2.7}$$

Since density variations are often caused by temperature or salinity, which are quantities that diffuse, it is often appropriate to require

$$\frac{D\rho}{Dt} = \kappa\nabla^2\rho, \tag{2.8}$$

where κ represents some ad hoc diffusivity. In light of our continuity equation, Eq. (2.1a) implies

$$\nabla\cdot\mathbf{u} = -\frac{\kappa}{\rho}\nabla^2\rho. \tag{2.9}$$

Since κ is typically very low, taking it into account is often irrelevant. The compressibility effects required in the Boussinesq approximation through κ to form a energetically consistent system are of little importance in most problems and shall therefore be neglected [4]. Although it is *energetically inconsistent with the Boussinesq approximation*, the continuity equation *will safely be assumed to be*

$$\nabla\cdot\mathbf{u} = 0. \tag{2.10}$$

From Eqs. (2.8), (2.9), (2.10), we eventually add the following consistent thermodynamic equation:

$$\frac{D\rho}{Dt} = 0. \tag{2.11}$$

Considering *small perturbations* of the velocity, buoyancy and pressure $u,v,w,b,p' = O(\varepsilon)$ ($|\varepsilon| \ll 1$), we linearize the continuity, momentum and energy equations Eqs. (2.10), (2.6), (2.11) and arrive to the following linear Boussinesq model:

$$\frac{\partial u}{\partial t} - fv = -\frac{1}{\rho_0}\frac{\partial p'}{\partial x} \tag{2.12a}$$

$$\frac{\partial v}{\partial t} + fu = -\frac{1}{\rho_0}\frac{\partial p'}{\partial y} \tag{2.12b}$$

$$\frac{\partial w}{\partial t} = -\frac{1}{\rho_0}\frac{\partial p'}{\partial z} + b \tag{2.12c}$$

$$\frac{\partial u}{\partial x} + \frac{\partial v}{\partial y} + \frac{\partial w}{\partial z} = 0 \tag{2.12d}$$

$$\frac{\partial b}{\partial t} + N^2 w = 0 \tag{2.12e}$$

where the Brunt-Väisälä (or stratification) frequency N is defined by

$$N^2 = -\frac{g}{\rho_0}\frac{\partial\bar{\rho}}{\partial z}. \tag{2.12f}$$

This measure of the stratification represents the natural oscillating frequency of a small parcel of fluid whose vertical position is slightly perturbed around its equilibrium ($\partial\bar{\rho}/\partial z < 0$).

Assuming an infinite domain in all directions, solutions of these linear system with constant coefficients (assuming $N = \text{const.}$) may be sought in the form of plane waves $q(\mathbf{x},t) = \tilde{q}(\mathbf{k})\exp[i(\mathbf{k}\cdot\mathbf{x} - \omega t)] + \text{c.c.}$ This assumption is justified if we investigate systems in which the vertical scale of stratification is much larger than the wavelenghts of interest. Eqs. (2.12) then take the matrix form

$$\begin{pmatrix} -i\omega & -f & 0 & \frac{ik}{\rho_0} & 0 \\ f & -i\omega & 0 & \frac{il}{\rho_0} & 0 \\ 0 & 0 & -i\omega & \frac{im}{\rho_0} & -1 \\ ik & il & im & 0 & 0 \\ 0 & 0 & N^2 & 0 & -i\omega \end{pmatrix} \cdot \begin{pmatrix} \tilde{u} \\ \tilde{v} \\ \tilde{w} \\ \tilde{p} \\ \tilde{b} \end{pmatrix} = \begin{pmatrix} 0 \\ 0 \\ 0 \\ 0 \\ 0 \end{pmatrix}, \tag{2.13}$$

where $\mathbf{k} = (k,l,m)$. Non-zero solutions are classically obtained by requiring that the determinant of the matrix is zero, giving the following dispersion relation:

$$\omega^2 = N^2 \frac{k^2+l^2}{|\mathbf{k}|^2} + f^2 \frac{m^2}{|\mathbf{k}|^2}. \tag{2.14}$$

Using this relation, we can easily show that $f < |\omega| < N$ for $N > f$, while $N < |\omega| < f$ for $N < f$, which constitutes the first property of internal waves. A second strong property can readily be highlighted in the limit where stratification dominates over rotation ($N > f$), as is typically the case in the ocean at mid-latitudes (we recall $f = 2\Omega \sin\theta_0$). In this case, the wave frequency does not depend on $|\mathbf{k}|$: taking θ as the angle of $\mathbf{k}$ with respect to the (k,l) plane yields $\omega = \pm N \cos\theta$. Let us now for simplicity rotate the x and y axis so that $\mathbf{k}$ is contained in the (x,z) vertical plane (with $l = 0$, $\partial/\partial y = 0$ for all fields). The next important feature of internal waves concerns the group velocity $\mathbf{c}_g$ at which their energy propagates. We have

$$\mathbf{c}_g = \nabla_{\mathbf{k}}\omega = \begin{pmatrix} \frac{\partial\omega}{\partial k} \\ \frac{\partial\omega}{\partial m} \end{pmatrix} = \begin{pmatrix} c_\phi \tan\theta \sin\theta \\ -c_\phi \sin\theta \end{pmatrix}, \tag{2.15}$$

with the phase velocity $\mathbf{c}_\phi = \omega\mathbf{k}/|\mathbf{k}|^2$, which yields $\mathbf{c}_g \cdot \mathbf{c}_\phi = 0$. This demonstrates that energy always travels perpendicularly to phase, or parallel to wavefronts, and that the energy of waves with positive vertical wavenumbers is radiated downwards ($c_{gz} < 0$) and vice-versa. Thus it follows from Eq. (2.15) that *phase and energy always propagate in the same horizontal direction, but opposite vertical direction*. Examination of the continuity and momentum equation reveals that $\mathbf{u} \parallel \mathbf{c}_g$ and that velocity and pressure oscillate in quadrature with buoyancy (crests and throughs of buoyancy are associated with zero velocity); internal waves are thus *transverse waves*. To conclude on the basic properties of internal waves, let us investigate two extreme cases. First, horizontal waves ($\theta \approx 0$) oscillate at high frequency $\omega \approx \pm N$, but they do not involve horizontal nor pressure oscillations ($u, p \approx 0$); the motion is purely vertical and the waves do not radiate energy ($\mathbf{c}_g \approx 0$). By contrast, the case in which $\theta \approx \pi/2$ is characterized by a zero phase speed (i.e. no wave motion): each horizontal sheet moves in a purely horizontal fashion at their own speed. This phenomenon may be thought of as the stratified analogue of Taylor's columns in rotating fluids [5].

2.3 Generation of internal tides

In this section, we explain how the interaction of tidal flows with the seafloor topography (hereafter called *bathymetry*) generates internal tides. We next focus on how those waves propagate and the vertical energy flux that they generate. These notions will set the framework in which we shall then study wave breaking responsible for energy dissipation and mixing.

The generation of internal tides has first been solved by Bell [6], who considered the ideal case of a 2D harmonic flow $U(t) = U_0 \cos(\omega_0 t)$ along x of a non-rotating, stably stratified fluid ($f = 0$, $N = \text{const.}$) of semi-infinite vertical extent. An obstacle $z = h(x)$ of characteristic length L and height h_0 perturbs the flow (see

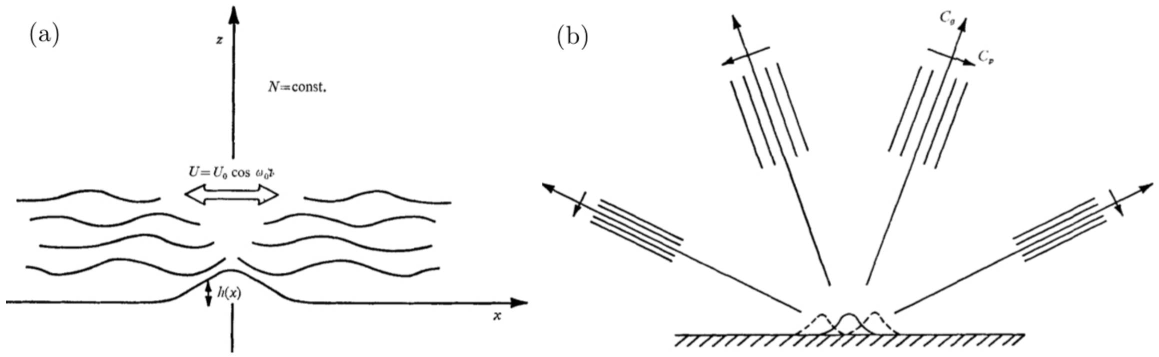

FIG. 2.2: (a) Definition sketch of tidal flow of a stratified fluid over an obstacle. (b) Schematic representation of the maximum excursion of the obstacle and induced wave fields. Energy propagates along long arrows (c_g), phase along short arrows (c_p). Reproduced from [6].

Fig. 2.2a). The corresponding set of linearized equations for the perturbations (u, w, p', b) is

$$\begin{aligned} \frac{\partial u}{\partial t} + U\frac{\partial u}{\partial x} &= -\frac{1}{\rho_0}\frac{\partial p'}{\partial x}, && (2.16a)\\ \frac{\partial w}{\partial t} + U\frac{\partial w}{\partial x} &= -\frac{1}{\rho_0}\frac{\partial p'}{\partial z} + b, && (2.16b)\\ \frac{\partial u}{\partial x} + \frac{\partial w}{\partial z} &= 0, && (2.16c)\\ \frac{\partial b}{\partial t} + U\frac{\partial b}{\partial x} + N^2 w &= 0. && (2.16d) \end{aligned}$$

Eq. (2.16) may be reduced to a single relation for the vertical velocity

$$\mathscr{D}^2\nabla^2 w + N^2\frac{\partial^2 w}{\partial x^2} = 0, \quad \text{with} \quad \mathscr{D}(t) = \frac{\partial}{\partial t} + U(t)\frac{\partial}{\partial x}, \tag{2.17}$$

and $\nabla^2 = \partial^2/\partial x^2 + \partial^2/\partial z^2$. The solution is assumed to be periodic in both x and t and the boundary condition in z is taken as

$$w(x, z = 0, t) = U(t)\frac{dh}{dx}(x). \tag{2.18}$$

This condition constraints the flow to be tangential to the undulating bathymetry. Prescribing the value of w at the bottom $z = 0$ is only valid provided that the slope of the emitted wave rays is much greater than the characteristic obstacle slope ($h_0/L \ll 1$). In the following, we shall restrict our attention to such *subcritical bathymetries*. The impact of finite subcritical slopes ($h_0/L < 1$) is thought to remain not too large, as summarized in [7]. Applying a Fourier transform in x to Eq. (2.17) yields

$$\widehat{\mathscr{D}}^2\frac{\partial^2\widehat{w}}{\partial z^2} - k^2(N^2 + \widehat{\mathscr{D}}^2)\widehat{w} = 0, \quad \text{with} \quad \widehat{\mathscr{D}}(t) = \frac{\partial}{\partial t} + ikU(t). \tag{2.19}$$

Following Bell [6], we switch to the frame moving with the tide by introducing the variable $\xi = x - \int_0^t U(\tau)\,\mathrm{d}\tau$. We further write $\widehat{w} = \widetilde{w}\exp[-ik\int_0^t U(\tau)\,\mathrm{d}\tau]$ such that $(1/2\pi)\int_{-\infty}^{+\infty}\widetilde{w}(k, z, t)\exp(ik\xi)\,\mathrm{d}k = w(x, z, t)$. The boundary condition Eq. (2.18) can then be expressed as

$$\begin{aligned} \widetilde{w}(k, 0, t) = \hat{h}\frac{\partial}{\partial t}\exp\left(+ik\int_0^t U(\tau)\,\mathrm{d}\tau\right) &= \hat{h}\frac{\partial}{\partial t}\exp\left(i\frac{kU_0}{\omega_0}\sin(\omega_0 t)\right)\\ &= \hat{h}\frac{\partial}{\partial t}\sum_{-\infty}^{+\infty} J_n\left(\frac{kU_0}{\omega_0}\right)\exp(in\omega_0 t)\\ &= \hat{h}\sum_{-\infty}^{+\infty}(in\omega_0)J_n\left(\frac{kU_0}{\omega_0}\right)\exp(in\omega_0 t) \end{aligned} \tag{2.20}$$

The solution is sought as follows:

$$\widetilde{w}(k,z,t)=\hat{h}(k)\sum_{-\infty}^{+\infty}\widetilde{W}_n(k,z)J_n\Big(\frac{kU_0}{\omega_0}\Big)\exp(in\omega_0 t), \tag{2.21}$$

where, due to the new reference frame, the $\widetilde{W}_n$ now satisfy the simple *autonomous* differential equation

$$\frac{d^2\widetilde{W}_n}{dz^2}+k^2\Big(\frac{N^2}{n^2\omega_0^2}-1\Big)\widetilde{W}_n=0, \quad \widetilde{W}_n(k,0)=in\omega_0. \tag{2.22}$$

This is trivially solved by

$$\widetilde{W}_n=in\omega_0\exp(ik\mu_n z), \quad \text{with} \quad \mu_n^2=\frac{N^2}{n^2\omega_0^2}-1. \tag{2.23}$$

Due to the nonlinear wave-flow interactions represented by the convective terms $U\partial u/\partial x$ and $U\partial w/\partial x$, the solution is not only composed of waves at the fundamental frequency ω_0, but *also of higher-order harmonics* $n\omega_0$. Oscillatory motions (as opposed to evanescent waves) are observed under the cut-off condition $n<N/\omega_0$ ($n\lesssim 5$ in the ocean for the semi-diurnal tide). We shall denote by $n_0=\lfloor N/\omega_0\rfloor$ the largest integer respecting the cut-off condition. Fig. 2.2b sketches sets of emitted rays of two different frequencies (e.g. ω_0 and $2\omega_0$). The slope of the characteristics along which energy radiates is given by μ_n^{-1}. The notion of causality imposes that the energy of the internal tides generated at the bottom can only propagate upwards. We therefore impose a *radiation condition* which should render the sign of the vertical component of the group velocity determinate, and namely positive. This is equivalent to imposing the sign of μ_n, which can be shown to yield

$$\operatorname{sgn}\mu_n=\operatorname{sgn}n. \tag{2.24}$$

Eventually, the general solution found by Bell [6] is

$$w(x,z,t)=-\sum_{n=1}^{n_0}\frac{n\omega_0}{\pi}\operatorname{Im}\left[\int_{-\infty}^{+\infty}\hat{h}(k)J_n\Big(\frac{kU_0}{\omega_0}\Big)\exp\Big(i(k\xi+\mu_n kz+n\omega_0 t)\Big)\right]. \tag{2.25}$$

The other wave fields u,p',b may be deduced by simple manipulations of the Fourier transformed Eqs. (2.16). The time-averaged upward energy flux E represents the conversion rate of the tidal power into internal tide. It is commonly expressed in W m^{-2}, and is defined as

$$E(z=0)=\left\langle\int_{-\infty}^{+\infty}p'(x,0,t)w(x,0,t)\,\mathrm{d}x\right\rangle=\left\langle\frac{1}{2\pi}\int_{-\infty}^{+\infty}\hat{p}(k,0,t)\hat{w}^*(k,0,t)\,\mathrm{d}k\right\rangle. \tag{2.26}$$

with $\langle\cdot\rangle$ denoting the time average over one period. The second equality comes from Parseval's theorem.

Bühler & Muller [8] extended Bell's model to three dimensions and rotating fluids ($f\neq 0$). For 2D seafloors, we represent the tidal forcing by a *tidal ellipse* of equation $\mathbf{U}(t)=[U_0\cos(\omega_0 t),V_0\sin(\omega_0 t),0]$. U_0 is the velocity along the major axis, while V_0 is the velocity along the minor axis. This ellipse is completely characterized by a third parameter, the angle α that the major axis makes with the x axis, see Fig. 2.3. In the rotated frame of the tidal ellipse the wave vector reads $(K,L)=(k\cos\alpha-l\sin\alpha,k\sin\alpha+l\cos\alpha)$. Neglecting the convective term in Eq. (2.16) requires the excursion parameter $\zeta=U_0/(\omega_0 L)$ to be much smaller than 1. In this *small excursion approximation*, only waves at the fundamental frequency ω_0 are generated and $J_1(U_0k/\omega_0)\approx U_0k/(2\omega_0)$. As the excursion parameter is not typically that small in our case, we *cannot* afford this approximation. However, it has been argued [9] that the linear solution for arbitrary excursion may still neglect higher-order harmonics $n\omega_0$,

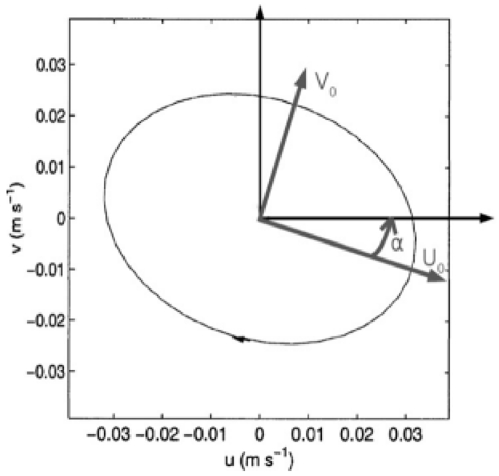

FIG. 2.3: Tidal ellipse example. U_0 and V_0 are the semi-major and semi-minor axis velocity respectively. α is the angle describing the ellipse orientation, here counterclockwise to East.

because solutions at the fundamental frequency ω_0 actually dominate the wave field. We shall therefore do so, but we take care to retain the full Bessel function in the amplitude instead of its asymptotic approximation. To study wave instabilities, it is useful to consider stratification surfaces of constant total buoyancy $\Theta = N^2 z + b$ (later referred to as *isopycnals*). Without waves, $b = 0$ and $\partial\Theta/\partial z = N^2$. If we denote by η the vertical perturbation displacement of such a surface, we have

$$\frac{\partial \eta}{\partial t} = w = -\frac{1}{N^2}\frac{\partial b}{\partial t} \tag{2.27}$$

using Eq. (2.16d) in the small excursion limit. This yields,

$$\frac{\partial \Theta}{\partial z} = N^2\Big(1 + \frac{1}{N^2}\frac{\partial b}{\partial z}\Big) = N^2\Big(1 - \frac{\partial \eta}{\partial z}\Big). \tag{2.28}$$

We introduce the nondimensional spatial wave field $A = \partial\eta/\partial z$ such that

$$\frac{\partial \Theta}{\partial z} = N^2\Big(1 - \mathrm{Re}[A(\mathbf{x},z)\mathrm{e}^{-i\omega_0 t}]\Big), \tag{2.29}$$

where now $\mathbf{x} = (x,y)$. As explained above, we only account for oscillations at the fundamental frequency ω_0.

The solution of Muller & Bühler [9] is expressed in terms of $\hat{A}(\mathbf{k}, z = 0)$ [with $\mathbf{k} = (k,l)$] and reads

$$\hat{A}(\mathbf{k},0) = 2i\kappa\mu\hat{h}(\mathbf{k})J_1\left(\frac{\sqrt{U_0^2K^2+V_0^2L^2}}{\omega_0}\right)\left(\frac{U_0K+iV_0L}{\sqrt{U_0^2K^2+V_0^2L^2}}\right)\mathrm{e}^{iV_0L/\omega_0}, \tag{2.30}$$

where $\kappa = |\mathbf{k}| = \sqrt{k^2+l^2}$ and we recall that

$$\mu = \sqrt{\frac{N^2-\omega_0^2}{\omega_0^2-f^2}}. \tag{2.31}$$

Any wave field can then be computed from $\hat{A}$ by the following so called *polarization relations*:

$$\hat{U} = \frac{\omega_0 k + ifl}{\kappa^2}\hat{A}, \quad \hat{V} = \frac{\omega_0 l - ifk}{\kappa^2}\hat{A}, \quad \hat{W} = \frac{\omega_0}{\mu\kappa}\hat{A}, \quad \hat{P} = \frac{\rho_0(\omega_0^2-f^2)}{\kappa^2}\hat{A}, \quad \hat{B} = -i\frac{N^2}{\mu\kappa}\hat{A}. \tag{2.32}$$

In light of Eqs. (2.26), (2.30), (2.32), we can write $E(z=0)$ as:

$$\begin{aligned} E(z=0) &= \frac{1}{(2\pi)^2}\int_{-\infty}^{+\infty}\int_{-\infty}^{+\infty}\frac{1}{2}\mathrm{Re}(\hat{P}\hat{W}^*)\,\mathrm{d}k\,\mathrm{d}l \\ &= \frac{\rho_0\omega_0(\omega_0^2-f^2)}{2\mu(2\pi)^2}\int_{-\infty}^{+\infty}\int_{-\infty}^{+\infty}\frac{|\hat{A}|^2}{\kappa^3}\,\mathrm{d}k\,\mathrm{d}l \end{aligned} \tag{2.33}$$

which can be expanded as

$$E(z=0) = \frac{\rho_0\omega_0(N^2-\omega_0^2)^{1/2}(\omega_0^2-f^2)^{1/2}}{2\pi^2}\int_{-\infty}^{+\infty}\int_{-\infty}^{+\infty}\frac{J_1^2\Big(\sqrt{U_0^2K^2+V_0^2L^2}/\omega_0\Big)|\hat{h}(\mathbf{k})|^2}{\kappa}\,\mathrm{d}k\,\mathrm{d}l. \tag{2.34}$$

Derived using a linear theory for the generation of internal tide, Eqs. (2.29), (2.30), (2.33) will form the basis of our future work.

2.4 Wave propagation in the inhomogeneous ocean interior

The oceans are not uniformly stratified. In addition to longitude and latitude, N indeed strongly depends on depth. It is usually minimum at the bottom of order $O(10^{-4}-10^{-3})$ s^{-1} and increases relatively modestly with height (typically one order of magnitude or less) up to a few hundred meters below the surface. Then, a strong upwards temperature gradient in the layers situated at $O(100)$ m below the surface (the so-called *thermocline*) is responsible for an abrupt increase of N to $O(10^{-2})$ s^{-1}. In general, the strong wind-induced mixing occurring in the few meters below the surface makes N decrease again. The propagation of internal waves depends very sensitively on the stratification of the supporting medium. In our work, we shall deal with global three dimensional stratification data. This section thus describes the Wentzel-Kramers-Brillouin (WKB) theory used to describe wave propagation in an inhomogeneous medium where $N=N(z)$.

We come back to the wave equation Eq. (2.22) which now has nonconstant coefficients. In the 3D, rotating case, for the first harmonic, it reads

$$\widetilde{W}''(z)+m^2(z)\widetilde{W}(z)=0, \quad \text{with} \quad m^2(z)=-k^2\Big(\frac{N^2(z)-\omega_0^2}{\omega_0^2-f^2}\Big). \tag{2.35}$$

The WKB approximation consists in postulating for $\widetilde{W}$ a slowly varying *complex* phase of the following form:

$$\widetilde{W}(z)\sim\exp\Big[i\Big(\frac{\phi_0(z)}{\varepsilon}+\phi_1(z)+O(\varepsilon)\Big)\Big] \quad \text{and} \quad m^2(z)=\frac{m_0^2(z)}{\varepsilon^2}. \tag{2.36}$$

where $\varepsilon \ll 1$ and $\phi_0,\ \phi_1\in\mathbb{C}$. Differentiating twice, we have

$$\widetilde{W}''(z)\sim\Big(-\frac{(\phi_0')^2}{\varepsilon^2}+i\frac{\phi_0''}{\varepsilon}-2\frac{\phi_0'\phi_1'}{\varepsilon}+i\phi_1''-(\phi_1')^2\Big)\exp\Big[i\Big(\frac{\phi_0(z)}{\varepsilon}+\phi_1(z)+O(\varepsilon)\Big)\Big]. \tag{2.37}$$

Eq. (2.36) can be rewritten order by order and yields the following:

$$O\Big(\frac{1}{\varepsilon^2}\Big) \quad : \quad -(\phi_0')^2=-m_0^2 \quad \Longrightarrow \quad \phi_0(z)=\int_0^z m_0(z)\,dz, \tag{2.38a}$$

$$O\Big(\frac{1}{\varepsilon}\Big) \quad : \quad i\phi_0''=2\phi_0'\phi_1' \quad \Longrightarrow \quad \phi_1'=\frac{i}{2}\frac{m_0'}{m_0} \quad \Longrightarrow \quad \phi_1(z)=i\ln\sqrt{\Big|\frac{m_0(z)}{m_0(0)}\Big|}. \tag{2.38b}$$

We conclude

$$\begin{aligned}\widetilde{W}(z) &\sim \exp\left[i\Big(\int_0^z \frac{m_0(z)}{\varepsilon}\,dz + i\ln\sqrt{\Big|\frac{m_0(z)}{m_0(0)}\Big|}\Big)\right] \\ &\sim \sqrt{\Big|\frac{m(0)}{m(z)}\Big|}\exp\left[i\Big(\int_0^z |m(z)|\,dz\Big)\right] \end{aligned} \tag{2.39}$$

In terms of the amplitude A, in the small excursion approximation we have $\hat{A} \approx \tilde{A}$, and using the polarization equation Eq. (2.32) (still valid at first order) we find

$$\hat{A}(\mathbf{k},z) = \hat{A}(\mathbf{k},0)\sqrt{\Big|\frac{m(z)}{m(0)}\Big|}\exp\left[i\Big(\int_0^z |m(z)|\,dz\Big)\right]. \tag{2.40}$$

The WKB approximation relies on the fact that the amplitude of the wave field varies one order more slowly than its phase. Note that this condition is not obvious from the expression Eq. (2.36) where imaginary phases must be seen as amplitudes (which is a powerful mathematical trick offering little physical understanding). Broadly speaking, the approximation is justified provided the scale over which the ambient N changes is larger than the vertical wavelength $1/m$. While this will be assumed to be the case in the deep ocean, it is not generally the case near the thermocline, where N'/N is much larger. However, as is often the case with asymptotic theory, the method provides a powerful approximation even outside its region of formal validity.

2.5 Instability, nonlinear wave breaking and mixing

Now that we can describe from linear theory the generation and propagation of internal tides, how can we predict the formation of instabilities dissipating a part of the power generated at $z = 0$? We shall discuss our next tool: how to use the linear theory to predict its own breakdown.

We recall Eq. (2.29), which expresses the vertical gradient of total buoyancy Θ in terms of a nondimensional amplitude A. Overturning of the surfaces of constant density (isopycnals) occurs when $\partial\Theta/\partial z < 0$, which is possible whenever $|A(\mathbf{x},t)| > 1$. This simple, yet highly physical criterion flags a so called *static instability*. This situation where a heavier fluid layer comes on top of a lighter one is known to be unstable and to lead to turbulent breaking. The choice of $|A| = 1$ as the critical value may be argued. Indeed, a wave can *dynamically* avoid breaking if a slight overturning $A \gtrsim 1$ occurs during a fraction of the wave period. We should therefore reformulate the static instability flag as $|A| = A_{\mathrm{sat}}$, with typically $A_{\mathrm{sat}} \approx 1 - 1.2$.

Bühler & Muller [8] showed that due to geometric focusing, high values of A may be reached locally far above the seafloor. In an effort to quantify the resulting wave instabilities and mixing, Muller & Bühler [9] derived a model for nonlinear wave breaking that our work will adopt. The idea is to iteratively propagate the wave field upwards using the linear theory under the constraint $|A| \leq A_{\mathrm{sat}}$. We impose this condition at each level assuming that the field is then stable and can be propagated further. This so-called *saturation scheme* is given by the following algorithm: (*i*) start at $z = 0$, (*ii*) saturate A at z, i.e. enforce $|A(\mathbf{x},z)| \leq A_{\mathrm{sat}}$ for all $\mathbf{x}$, (*iii*) propagate the saturated amplitude at level $z + dz$. The question that arise is: how do we impose the stability constraint once the instability criterion is exceeded? In other words: how is wave breaking parametrized?

The straightforward, yet unfortunately naive way to implement (*ii*) would be to saturate the amplitude by $A_s = A \times A_{\text{sat}}/|A|$ if $|A| > A_{\text{sat}}$, where the subscript denotes the saturated amplitude. This method however violates the zero (x,y)-mean property of the wavefield and disregards the global dependence of the other wave variables on A yielding nonphysical phenomena. For example, as we deal with incompressible flows, a local change on A can produce a global change on the pressure field. The authors instead proposed a localized saturation [9]:

$$A_s = A\left[1+\left(\frac{A_{\text{sat}}}{|A|}-1\right)\chi_{|A|>A_{\text{sat}}} * g\right] \quad \text{with} \quad \hat{g}(k,l) = \frac{\kappa^2}{\kappa^2 + L_{\text{sat}}^{-2}}. \tag{2.41}$$

This convolution with $g(x) = \delta(x) - \mathrm{e}^{-|x|/L_{\text{sat}}}/2L_{\text{sat}}$ (in 1D) does nothing more than subtracting a weighted local average, but the saturation length L_{sat} is an ad-hoc parameter to which we must give a value. Invoking physical arguments, it has been suggested to set L_{sat} to the value minimizing the bottom energy flux $E(z=0)$ (the authors found $L_{\text{sat}} = 5$ km), but this might be amended as we shall see. This saturation has the merit of being both advantageously simple and physical and of having been confirmed by numerical work and observations[10], which is why we shall use it in this work.

Since the saturation of A is nonlinear, it is not certain that the effect Eq. (2.41) is to decrease the total energy flux. Indeed, as we can see in Eq. (2.33), the flux E_s is proportional to the integral over the spectral space of $\hat{A}_s/\kappa^3$. The saturation does tend to make $\hat{A}_s$ less energetic, but its effect, rather in the real space, is highly nonlocal in the spectral space (uncertainty principle). Redistribution of a part of the energy of the spectrum $\hat{A}$ at lower wavenumbers κ may actually increase E_s, at least in theory. In the implementation of the scheme, we however observed that such cases were not common at all, and that such effects are always canceled by averaging over different wavefields in a statistical framework, which is the topic of the next section.

One of the main goal of this work is to produce a global map of the vertical energy dissipation rate (in W kg^{-1} or m^2 s^{-3}) given by

$$\varepsilon = -\frac{1}{\rho}\frac{\partial E_s}{\partial z}, \tag{2.42}$$

where E_s is the saturated energy flux, computed remplacing $\hat{A}(k,l,z)$ in Eq. (2.33) by $\hat{A}_s(k,l,z)$, the actual saturated amplitude at each altitude. Since mixing is a transfer of kinetic energy into potential energy, it is easy to conceive that less stratified fluids (with smaller N) mix more effectively under the action of a given ε. This is why the *diapycnal diffusivity* K_ρ, which directly expresses the *vertical mixing intensity*, is often considered in the literature. Osborn & Cox [12] proposed the following model:

$$K_\rho = \Gamma\frac{\varepsilon}{N^2}, \tag{2.43}$$

where Γ is a nondimensional turbulent mixing efficiency that they set to $\Gamma = 0.2$.

To summarize what we have seen up to now, Fig. 2.4 gives a first overview of the internal tide wave field generated by a given bathymetry, its vertical propagation and dissipation. For two different $N(z)$ profiles (constant in Fig. 2.4a, and real in Fig. 2.4b) a few isopycnals (isosurfaces of Θ) are depicted. The wave field that would

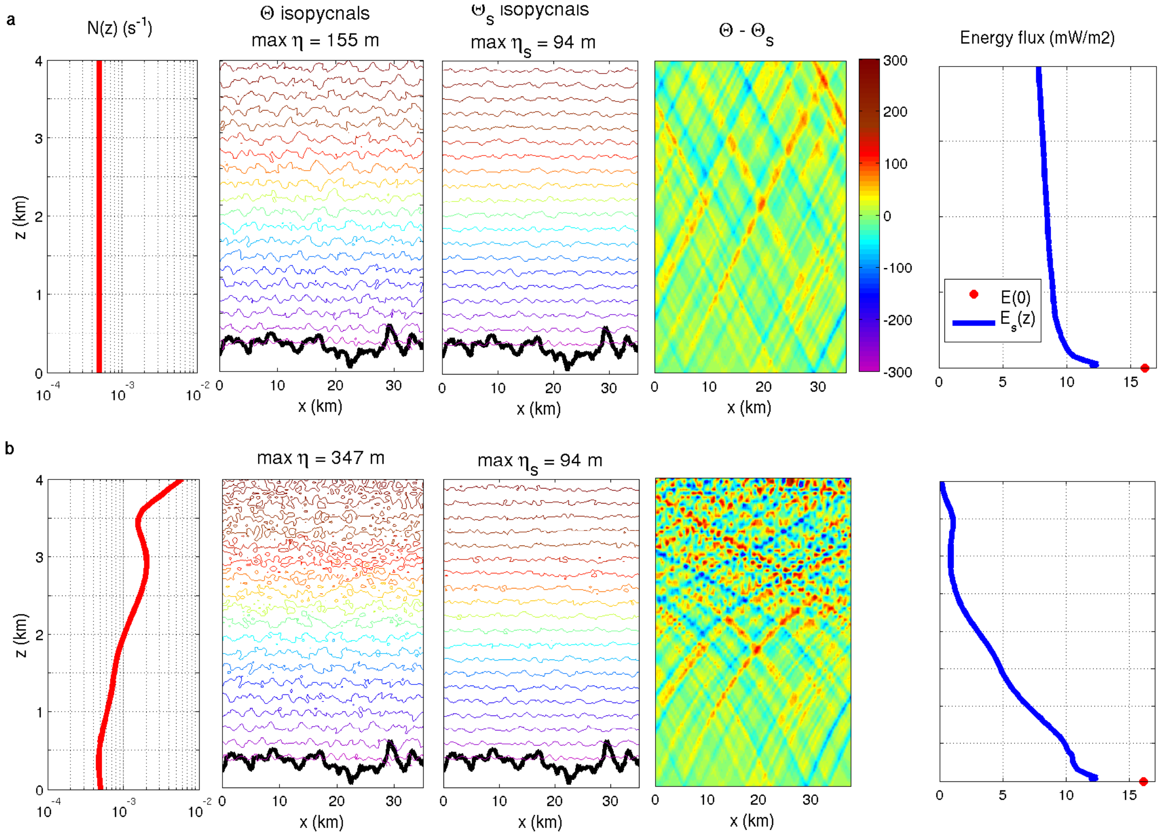

FIG. 2.4: Two-dimensional slices of isopycnals before (Θ) and after (Θ_s) saturation, their difference and the resulting energy flux with height. The bathymetry used for these calculations is shown in dark bold lines. Two stratifications are shown for comparison: (a) Unrealistic $N(z) = \text{const.}$ (b) Typical oceanic $N(z)$ profile.

exist without parametrizing wave breaking (i.e. $A_{\text{sat}} = \infty$) is compared with the "physical" field Θ_s that underwent multiple saturation steps (with $A_{\text{sat}} = 1$) from the bottom ($z = 0$ km) to the top of water column ($z = 4$ km). To see this effect, the difference is plotted. Finally, the energy flux shows how saturation reduces the upward energy flux by dissipating it into local turbulence. We see that the bottom field is heavily saturated, resulting in a large energy loss (from $E(0) \approx 16$ mW m^{-2}, see the red dot, to $E_s(0) \approx 12$ mW m^{-2} the start of the blue curve). The maximum isopycnal displacement η_s of the stable field being equal to 94 m in both cases, it is very likely attained at the bottom (since above the bottom, both fields start to differ). The next obvious observation is that the stable field displays much less overturning than the initial one, especially in case b (where max η is almost three times as large as in case a). Locations where the saturation induces the largest differences are visible in the form of rays on the $\Theta - \Theta_s$ plot. They originate from points where the bathymetry has high gradients $|\nabla h|(x,y)$ and propagate along characteristics of slope μ^{-1} in case a, according to the linear theory. In case b, the WKB theory takes into account the decreasing slope $\mu^{-1} \propto 1/N$ and the characteristics are curved, while the vertical spatial scales visibly decrease with the altitude. When characteristics cross, focusing occurs, generally increasing the local wave amplitude and resulting in greater dissipation. By reducing the ray slope, the increase of N above the bottom in case b enhances this crossing of characteristics and the concomitant dissipation. Indeed, while $E_s(4$ km$) \approx 8$ mW m^{-2} in case a, almost all the energy is lost in case b when the field reaches the sea surface level [$E_s(4$ km$) \approx 0$ mW m^{-2}].

2.6 Statistical modelling of small-scale bathymetry

In the previous sections, we have seen that the vertical structure and energy flux of the waves above a given seafloor topography (bathymetry) $h(\mathbf{x})$ [here $\mathbf{x} = (x,y)$] could be deduced by successive steps of upward propagation and saturation of the solution generated linearly at the seafloor. We need global bathymetric data, but we are aware of the large range of potential lengthscales (the seafloor has a fractal structure) and the technical difficulty to obtain accurate measurements at such abyssal depths. We must therefore answer the question: which bathymetric lengthscale participates the most to unstable internal tides and how to represent such data?

The two most relevant features of the seafloor for us are *canyons*, typically of horizontal length $O(10-100)$ km, and *abyssal hills*, with smaller scales about $O(0.1-10)$ km. Abyssal hills are generally found around regions separating tectonic plates. The height of this gentle fabric is typically between $O(10-100)$ m and rarely exceeds a few hundred meters. Intense volcanic activity generates new crustal material at spreading ridges, where plates diverge at a rate of $O(1)$ cm year^{-1}. This accretion generates rough seafloors, over which sediments are gradually deposited with time. Due to this increasing sediment cover, roughness generally decreases away from the ridge and even vanishes in vast parts of the deep ocean (see Fig. 2.5).

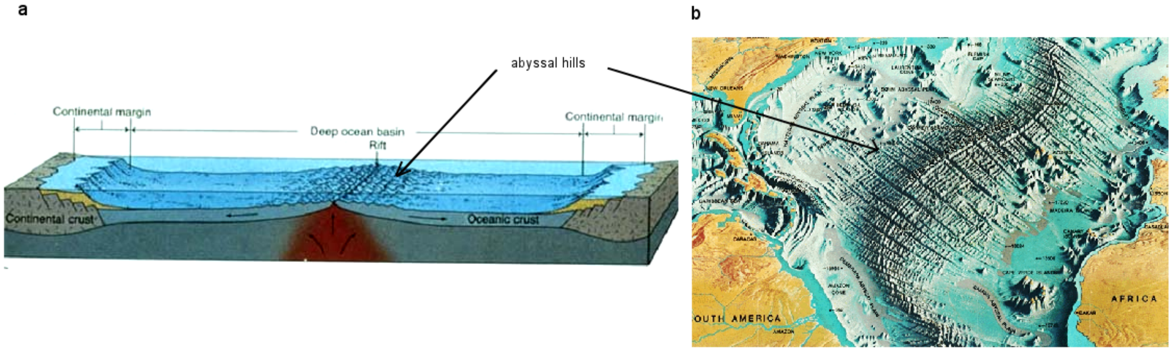

FIG. 2.5: (a) Schematic side view of a deep ocean basin and a continental margin. A spreading ridge at the center, active for millions of year, is at the origin of rough abyssal hills surrounding it. (b) Top view of the northern part of the Mid-Atlantic Ridge, separating Africa and Europe from America. A vast region of hills can be seen away from the rift. Adapted from [14].

Scales shorter than 100 m in length have little impact on wave radiation. Indeed, from Eq. (2.34) we know that $E_0 \propto \int\int J_1^2(U\kappa/\omega_0)|\hat{h}(\mathbf{k})|/\kappa \, \mathrm{d}k \, \mathrm{d}l$: smaller scales do not contribute much to the flux (for excursions $2\pi\zeta = U\kappa/\omega_0 \gg 3/4$, the integrand behaves as $\propto |\hat{h}(\mathbf{k})|/\kappa^2$, favoring large scales). On the other hand, scales larger than $O(50)$ km are simply not radiated [13]. To understand why, we must relax the assumption of a semi-infinite ocean, which was initially used to study internal wave generation. After reflection of the wave by the sea surface, a regime of standing waves is established, and the longest wavelength that can be supported is $2H$ (H is the depth), corresponding to the first vertical mode. A wave with horizontal scale of 50 km has a vertical wavelength of 50 km $/\mu$, where typically $\mu \approx 5$. Such a wave is therefore only present in depths greater than 5 km. Further studies [11, 9] and suggested that features of scales $O(1)$ km were more prone to focusing leading to turbulent mixing than $O(50)$ km features. It therefore emerges that our model should focus on the description of abyssal hills, sustaining the largest part of energy dissipation, and include features of length scales $O(100)$

m $-$ $O(50)$ km. Unlike canyons which are well-described isolated features, abyssal hills are ubiquitous around spreading ridges and below the current resolution of satellite bathymetry. We must thus give up the illusory idea of a deterministic description of the bathymetry and use a statistical approach instead.

The common statistical model proposed by Goff and Jordan [15] models the abyssal hills as a Gaussian random field. The stochastic signal $h(\mathbf{x})$ is defined to have zero mean [$\mathbb{E}(h(\mathbf{x}))=0$, where $\mathbb{E}$ denotes the expected value operator] and to be stationary, which makes it fully determined by its two-point covariance function

$$C_{hh}(\mathbf{x}) = \mathbb{E}\Big[h(\xi)h(\xi+\mathbf{x})\Big]. \tag{2.44}$$

The total bathymetric variance is $H^2 = C_{hh}(0)$ and it is assumed that far from characterizing all the seafloor features, second-order statistics already capture some salient features. Goff and Jordan adapted a von Kármán spectral model anisotropic in form characterized by five parameters, including H. To be specific, the power spectrum of C_{hh}, hereafter noted $P_h = |\hat{C}_{hh}|^2$ is given by:

$$P_h(\mathbf{k}) = 4\pi\nu H^2 |\mathbf{Q}|^{-1/2}[u^2(\mathbf{k})+1]^{-(\nu+1)}. \tag{2.45}$$

where ν is the Hurst number, characterizing the power-law decay at high wavenumbers (fractal dimension is $D=3-\nu$) [15]. The symmetric and positive definite matrix $\mathbf{Q}$ and u are defined as:

$$\mathbf{Q} = k_n^2\mathbf{e}_n\mathbf{e}_n^T + k_s^2\mathbf{e}_s\mathbf{e}_s^T, \quad u(\mathbf{k}) = [\mathbf{k}^T\mathbf{Q}\mathbf{k}]^{1/2} = \sqrt{\left(\frac{\kappa}{k_n}\right)^2\cos^2(\theta-\theta_s)+\left(\frac{\kappa}{k_s}\right)^2\sin^2(\theta-\theta_s)}. \tag{2.46}$$

Here k_n^2, k_s^2, $\mathbf{e}_n$, $\mathbf{e}_s$, are respectively the eigenvalues ($k_n > k_s$), normalized (orthogonal) eigenvectors of $\mathbf{Q}$ and θ_s denotes the single angle characterizing the azimuth of $\mathbf{e}_s$ (direction of largest undulation) [16]. The power spectrum is flat at low wavenumbers and suddenly decays with exponent ν above the roll-off values k_n, l_n. The global maps that we shall use are reproduced in Fig. 2.6.

As described in the following chapter, our approach will be statistical and consist in (*i*) calculating P_h at a given location, (*ii*) generating random synthetic bathymetries constrained by this spectrum, (*iii*) determining the corresponding vertical mixing profile at this location, (*iv*) averaging over several bathymetry samples.

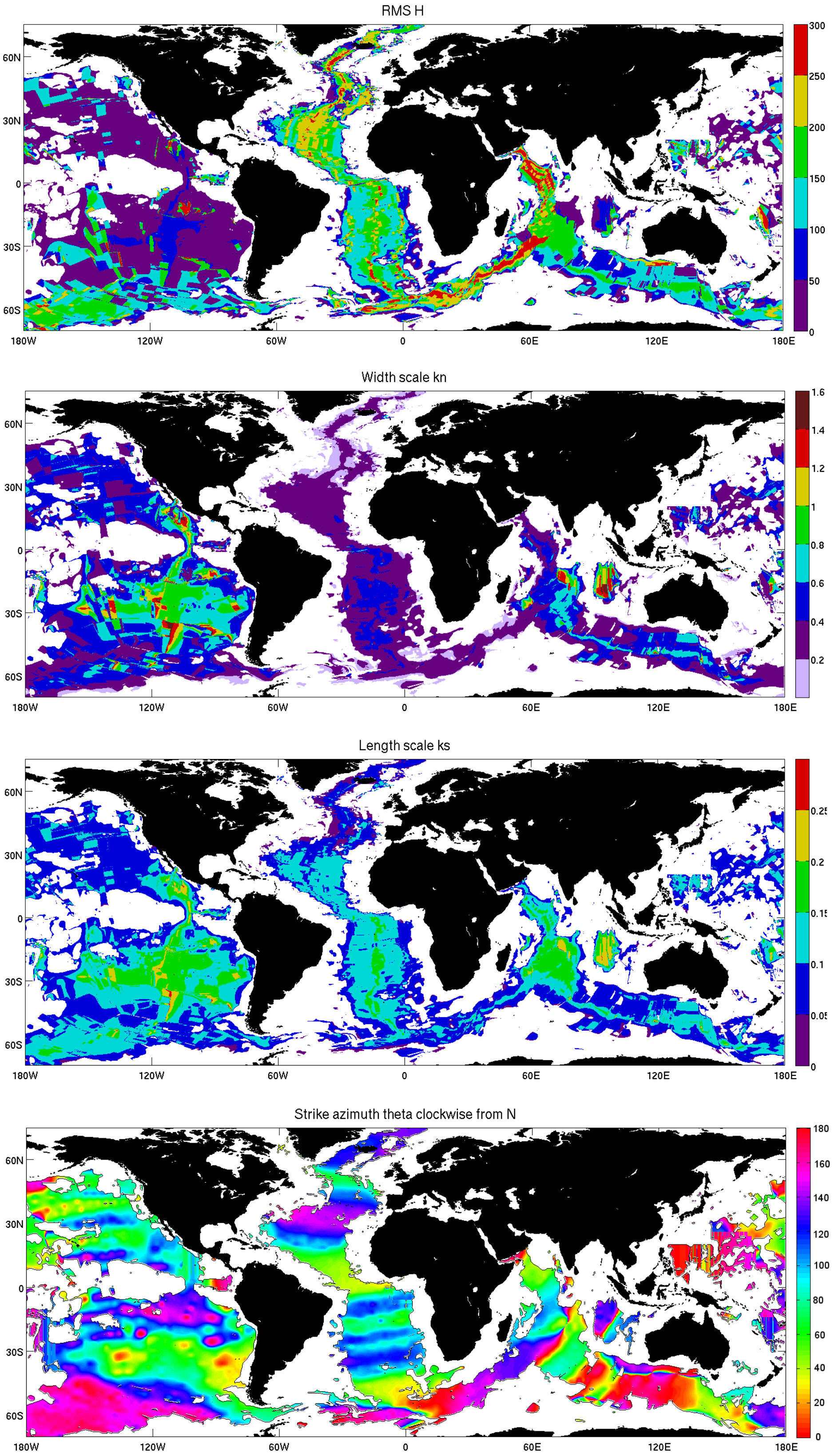

FIG. 2.6: Worldwide maps ($1/4^\circ \times 1/4^\circ$ resolution) of the spectrum parameters H (in m), k_n, k_s (in km^{-1}) and θ_s (clockwise from North) respectively (see text for description). The last parameter ν is omitted, its value being almost uniform $\nu \approx 0.9$ except in very localized areas. White indicates regions of no abyssal hills roughness (smooth sediment cover).

Chapter 3

Methods: numerical model and data

Now that we have discussed the theory underlying our model, we explain how to perform its numerical implementation. MATLAB was chosen for several reasons: (*i*) large portions of the code were already written in that language, (*ii*) it offers convenient built-in functions minimizing development time, and (*iii*) many graphical options and a friendly interface enable to interactively test the code and analyze results. In this chapter, we deal with some important issues that our problem involves, namely the generation of synthetic random bathymetries (Section 3.1) as well as spatial resolution, discretization and the choice of the free saturation length parameter L_{sat} (Section 3.2). We present the worldwide data for the tidal flows and 3D stratification used in this study in Section 3.3 and detail the full algorithm in Section 3.4.

3.1 Generation of synthetic random bathymetries

This section deals with the generation of abyssal hills bathymetry $h(\mathbf{x})$ from the power spectrum $P_h(\mathbf{k})$ given by Eqs. (2.45), (2.46) and Fig. 2.6 of their statistical covariance function Eq. (2.44).

At each grid point location ($1/4^\circ \times 1/4^\circ$ resolution in longitude and latitude), our approach consists in generating a number of synthetic bathymetric samples, whose properties are constrained by the local covariance (recall: the mean value of abyssal hill height is 0). Since we intend to average the mixing rates induced by the waves generated over many samples, it is highly desirable for the statistical properties of our results to generate bathymetries that are *independent* from each other. To do so, an efficient way is to consider the stationary complex Gaussian field $h = h_1 + ih_2$ with covariance $2C(x,y)$. By definition, h_1 and h_2 are independent, real-valued Gaussian fields with covariance $C(x,y)$ [18]. We compute $\hat{h}$ as follows:

$$\hat{h}(k,l) = L\sqrt{P_h(k,l)}\Big(A(k,l) + iB(k,l)\Big) \tag{3.1}$$

where L is the linear size in the physical domain (for a square box $L \times L$) and A, B are two independent Gaussian random fields $\sim \mathcal{N}(0,1)$ [17]. For the cost of a single inverse Fourier transform of $\hat{h}$, we eventually obtain by taking the real and imaginary part of h *two* independent bathymetry samples h_1 and h_2. Fig. 3.1 illustrates a typical real space synthetic bathymetry $h(x,y)$ obtained by the numerical implementation of this technique. Note the anisotropy of the roughness: while elongated features with long oscillations are found along the x axis (the so-called "strike axis"), we observe much smaller scale features along the y axis. Spectrally, this is explained by a higher roll-off wavenumber in the normal direction k_n than in the strike direction k_s. Finally, to show the success of the generation of random topographies, we computed the empirical power spectrum from fifty synthetic samples h. As shown in Fig. 3.2, the empirical spectrum agrees very well with the exact one (though convergence is faster in the strike direction) and this is why we conclude that our synthetic topographies indeed have the desired covariance properties.

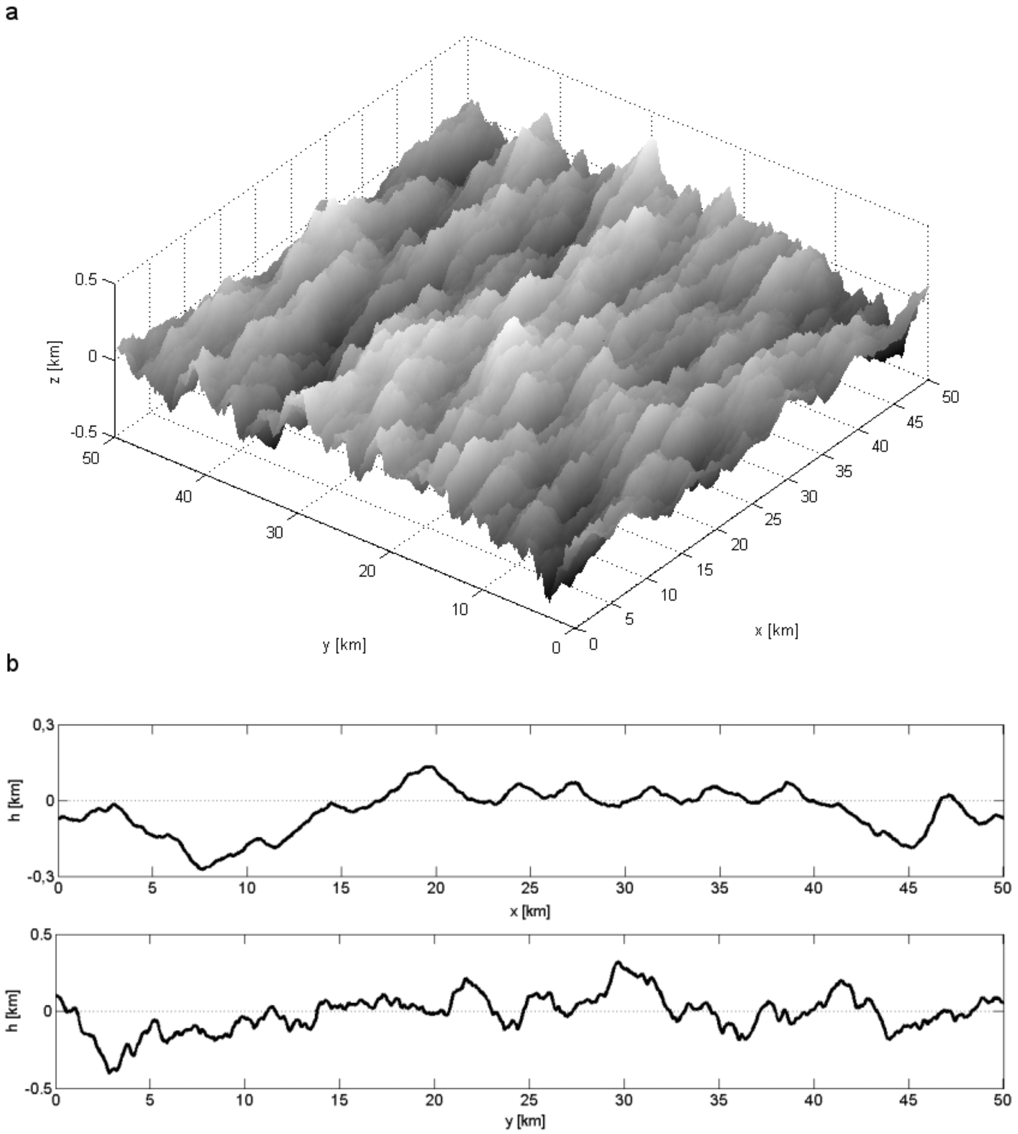

FIG. 3.1: Synthetic bathymetry obtained for $H = 0.11$, $k_s = 2\pi/26.6\ \mathrm{km}^{-1}$, $k_n = 2\pi/6.28\ \mathrm{km}^{-1}$, $\nu = 0.9$. Domain length is 50 km (not up to scale in z) and grid size ≈ 0.1 km ($2^9 = 512$ discretization points). (a) 2D view. (b) Arbitrary x and y cross-section. Note that the z scale is stretched for clarity (in the real scale, the bathymetry is mostly subcritical).

The linear theory for wave generation relies on the assumption that the bathymetry is subcritical: $\delta(x,y) = |\nabla h(x,y)|/\mu^{-1} < 1$. This guarantees that the emitted wave ray has a larger slope than the local bathymetry and that it is free to radiate upwards. In our framework, the expected supercritical parameter δ^2, is given in Fourier

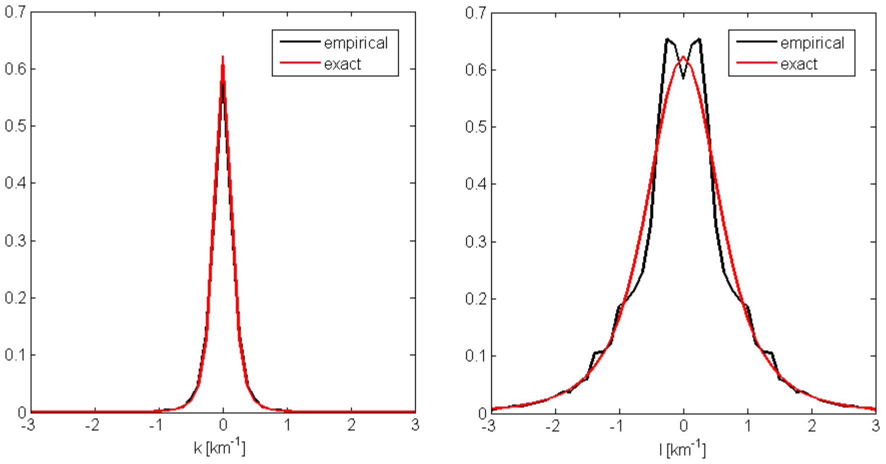

FIG. 3.2: Original (exact) power spectrum used in Fig. 3.1 and empirical average computed from 50 samples. Two cross-sections in the plane $l = 0$ (left) and $k = 0$ (right) are shown. We conclude that synthetic topographies approximately have the desired properties.

space by

$$\delta^2 = \mu^2\, \mathbb{E}(|\nabla h|^2) = \frac{\mu^2}{4\pi^2} H^2 \kappa^2. \tag{3.2}$$

To get rid of supercritical slopes, we choose to correct the power spectrum P_h if somewhere $\delta^2(k,l) > 1$, by applying the following *supercritical correction*:

$$P_h(k,l) \longleftarrow \frac{P_h(k,l)}{\delta^2(k,l)} \quad \text{where} \quad \delta^2(k,l) > 1. \tag{3.3}$$

This guarantees that the expected value of the slope of the bathymetric samples will be everywhere subcritical (though it may still locally be slightly supercritical).

We end this section with a short discussion about the length L that we will give to our square domain and the spatial resolution dx at which it is discretized. The first requirement is that the domain length be larger than the largest spatial scales contained in the spectrum, whose order of magnitude is given by the smallest roll-off wavenumber (in the strike direction) $2\pi/k_s$. Second, the smallest spatial scale that we are able to resolve ($2dx$ according to the Nyquist-Shannon condition) ought to be smaller than the smallest features described by P_h, hence $dx \ll 2\pi/k_n$. To provide a first rule of thumb for the value of these parameters, we carried out a sensitivity analysis on a good number of typical bathymetries. For each bathymetry, we separately increased L and decreased dx until convergence of the vertical profiles $E_s(z)$ was obtained. For the sake of brevity, the results are not reported here, but it emerged that values such as $L \gtrsim 1 \times (2\pi/k_s)$ and $dx \lesssim (1/40) \times (2\pi/k_n)$ constitute good rules of thumb. More accurate values will be given in the chapter devoted to our results, and a thorough sensitivity analysis to these parameters is conducted in Appendix A.

3.2 Optimal saturation length parameter

The next point that we shall discuss is the value of the free parameter L_{sat} (see Section 2.5), denoting the saturation length used in Eq. (2.41). In their article, Muller & Bühler [9] proposed to choose L_{sat} as the value that minimizes the saturated bottom energy flux $E_s(0)$, in consistency with the expectation that optimal saturation should yield the maximum decrease of energy. From their analysis with a specific bathymetry emerged the value $L_{\text{sat}} = 5$ km.

In our work, we will introduce a slightly different approach which has the merit of assigning an "optimal" L_{sat} to each bathymetry realization at very limited computational cost. The idea is to look directly at the bottom value of the wave field $A(x,y,0)$, and more specifically find its *most energetic spatial scale*. We first find (k_A, l_A) such that $\hat{A}(k,l,z=0)$ is maximum and deduce

$$L_A = \sqrt{\left(\frac{2\pi}{k_A}\right)^2 + \left(\frac{2\pi}{l_A}\right)^2} \tag{3.4}$$

This dominant length scale L_A (in the sense of maximum spectrum energy) will be used to determine L_{sat}. Imposing saturation at the most energetic length scale is indeed thought to maximize the dissipation at the bottom as well as for $z > 0$, which seems physically relevant. However, it is not completely clear how we should deduce L_{sat} from L_A. Allowing for L_{sat} to simply be a multiple of L_A: $L_{\text{sat}} = \gamma L_A$, we decided to investigate the sensibility of the value of γ for a single bathymetry, in order to find the optimal value of this parameter, with the objective to generalize to every bathymetry. Fig. 3.3 shows how the saturation of the bottom energy flux depends on γ. The

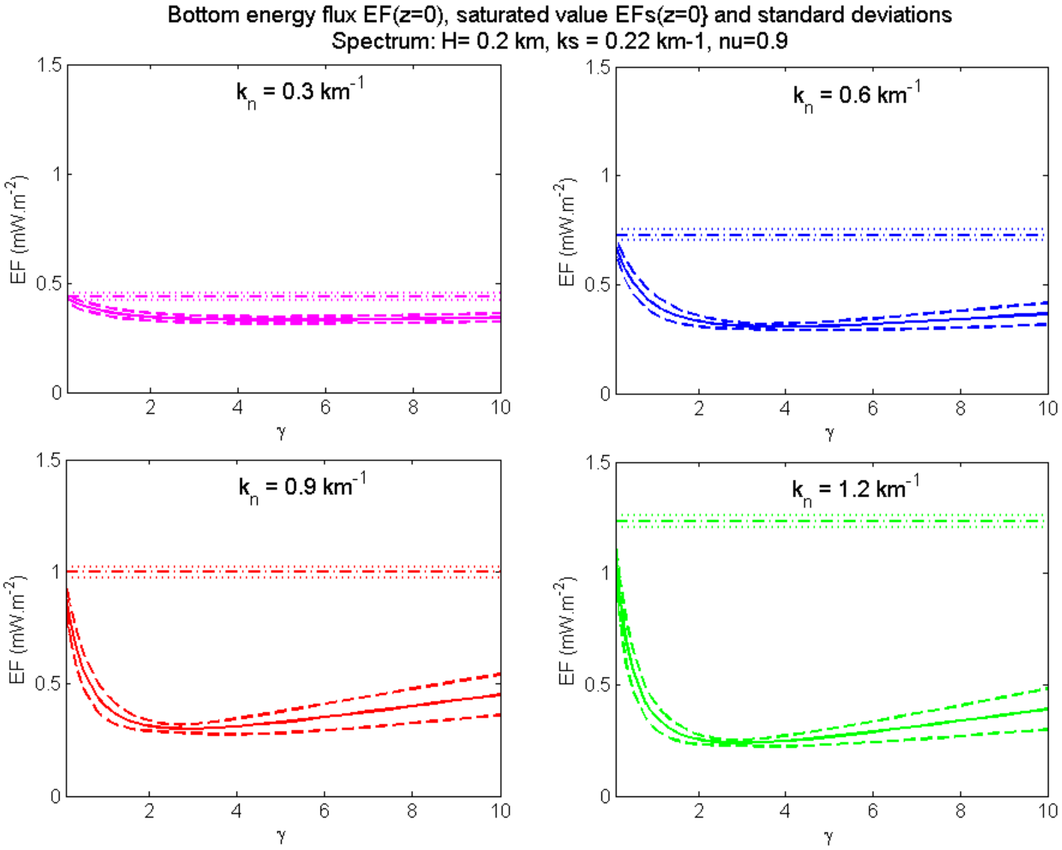

FIG. 3.3: Determination of the optimal γ parameter for the saturation length from saturated bottom energy flux. Minimum mean (—) and standard deviation (— —) of $E(z=0)$ indicate optimal γ. Values of E(0) (mean — · — and deviation · · ·) are just given for comparison. Results are reported for various topographic roughness k_n to show robustness.

results are shown for typical bathymetry spectra with increasing k_n values and have been averaged over several random samples for reliability (plotted as mean value ± standard deviation among the sample). For relatively smooth seafloors, γ has little influence (at least for the values $2 < \gamma < 10$) simply because no dissipation occurs. However, when nonlinear breaking increases as a result of smaller scale features (higher k_n), it becomes very clear that *there exists an optimal* γ *value* associated with minimum $E_s(0)$ values. In this case, we read $\gamma \approx 3$, which is the value will shall use in our work. Interestingly, this value does not depend on the different spectra, provided they contain sufficiently small scales (here $k_n \gtrsim 0.6\ \mathrm{km}^{-1}$), giving relative generality and robustness to this result. Also, this optimal γ value seems to correspond to minimum standard deviation, meaning that using this saturation length yields more repeatable results, or saturated values that have less variability when computed with different bathymetry samples from the same covariance spectrum. This feature represents another great advantage of this method. What is more, our method is computationally much more efficient than the one proposed in [9], which required to test several values and the computation of $E_s(0)$ for each of them. By contrast, we will simply determine for each bathymetry sample the length L_A (at no cost, since $\hat{A}$ is readily known at this stage), from which we directly deduce the optimal parameter

$$L_{\mathrm{sat}} = \gamma L_A = 3L_A. \tag{3.5}$$

In practice, we find that $L_{\mathrm{sat}} = O(1)$ km.

3.3 Tidal and stratification data

The worldwide computation of internal tides obviously requires the knowledge of the tidal currents wherever abyssal hills are present (see Fig. 2.6 for the cover). Barotropic tides (i.e. depth-independent tides) originate from the gravitational attraction of water masses by celestial bodies. The Moon and the Sun are responsible for most of the tides in the oceans, which are at each point, a superposition of motions of different amplitude, phase and frequency. At most locations however, the dominant tidal constituent turns out to be the *principal lunar semi-diurnal tide* (abbreviated M_2). It period is half a lunar day, that is $T_{M2} = 12$ hr 25.2 min. In our work, we will restrict our attention to the waves generated by this tidal harmonic, of single frequency $\omega_0 = 2\pi/T_{M_2} = 1.454 \times 10^{-4}\ \mathrm{s}^{-1}$.

As explained in Chap. 2, the most convenient way to represent tides in our wave theory is to use a tidal ellipse of parametric equation $\mathbf{U}(t) = [U_0 \cos(\omega_0 t), V_0 \sin(\omega_0 t), 0]$ and orientation α. The determination of U_0, V_0 and α has been made using the recent global model TPXO 7.2 developed by Egbert and Erofeeva [20]. This model has the same resolution as our bathymetry data (1/4 degree) and predicts most tidal constituents by assimilation of very accurate sea level data provided by the TOPEX/Poseidon satellite radar altimetry (see Fig. 3.4). This extremely successful satellite mission was the first to produce global coverage of the ocean surface bathymetry with a record precision of a few centimeters [19]. The inverse tide model TPXO 7.2, coupled with the Tide Model Driver (TMD) toolbox [20] enabled us to produce global maps of the M_2 ellipse parameters, as shown in Fig. 3.5.

The next step is to determine the global three-dimensional profiles of the stratification frequency $N(x,y,z)$. This has recently become possible with the data provided by the World Ocean Circulation Experiment (WOCE) [21]. Assimilating data from satellites and a wide network of buoys taking in situ measurements down to abyssal depths, this program provided us with 3D, year-averaged salinity and temperature data. This data enabled us to

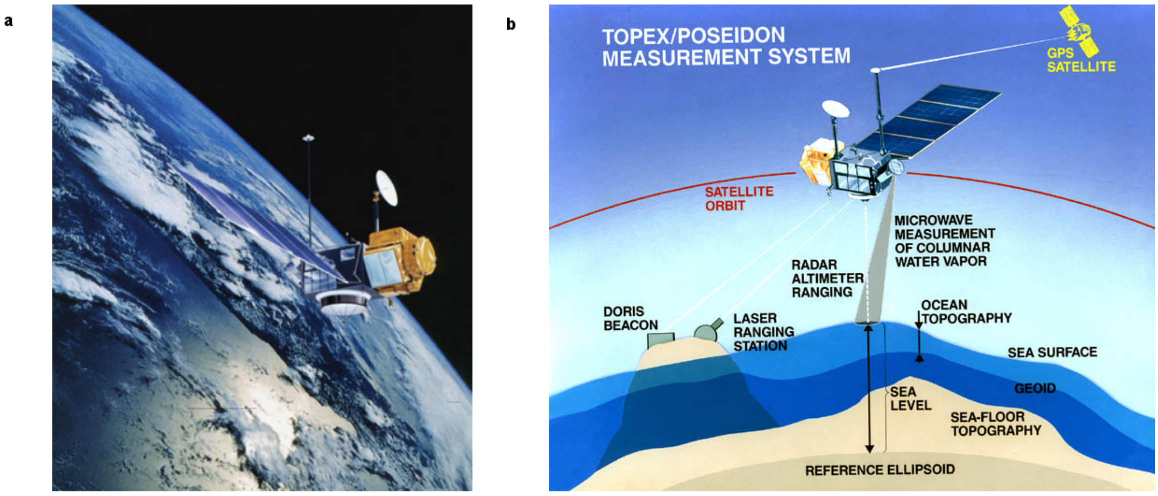

FIG. 3.4: (a) View of the TOPEX/Poseidon satellite orbiting 1,330 km above the Earth. (b) Schematic view of the measurement system, whose main component is the radar altimeter. Reproduced from [19].

compute the density, and by differentiation, the stratification frequency. The careful computation of $N(x,y,z)$ has been carried out using the Gibbs Seawater MATLAB Toolbox [22]. The map of the bottom frequency $N(x,y,z=0)$ is given in Fig. 3.6.

3.4 Complete algorithm

We now introduce in more details the procedure we use to compute the vertical energy flux profiles $E_s(z)$ in the whole water column [dissipation rate is deduced by differentiation as shown in Eq. (2.42)]. Propagation of the waves is normally carried out until the ocean surface, but if somewhere in the ocean interior the stratification becomes too weak $N(z) \leq \omega_0$, *the wave is reflected downwards* [23]. The propagation must then be stopped and the remaining energy is considered to radiate away without further dissipation. The algorithm is designed to loop over all available locations (not in white in the previous maps) and read topographic and physical data. At each location, the bathymetric spectrum is read, corrected if supercritical slopes are expected, and a number of samples N_{sample} (judged sufficient to yield reliable statistical estimates) are randomly generated. To prevent our results from being flawed by unrealistic values, we must impose a maximum value to the bottom amplitude. Indeed, as can be seen in Fig. 3.5, shallow regions may have exceptionally high tidal amplitudes which are unreliable (especially near Iceland). In the literature, this problem is solved by *imposing a capping value on the bottom flux* $E(0) \leq E_0^{\text{cap}}$ [28]. If the bottom flux exceeds the capping value, we impose $E(0) = E_0^{\text{cap}}$ by

$$\hat{A}(k,l,0) \longleftarrow \hat{A}(k,l,0) \times \left(\frac{E_0^{\text{cap}}}{E(0)}\right)^2 \tag{3.6}$$

The capping value and its influence will be discussed in the next chapter. The upward propagation of the wave field is carried out at discrete vertical intervals dz and each propagation step is followed by a saturation step. The calculation of $E_s(z)$ from $\hat{A}_s(z)$ is done as in Eq. (2.33) (where $\hat{A}$ must be replaced by $\hat{A}_s$. Obviously, the integral with infinite bounds is symbolic; the numerical integration requires a discrete summation over a finite spectral domain determined at the beginning of the algorithm. Now that we introduced all the necessary ingredients, the algorithm reads:

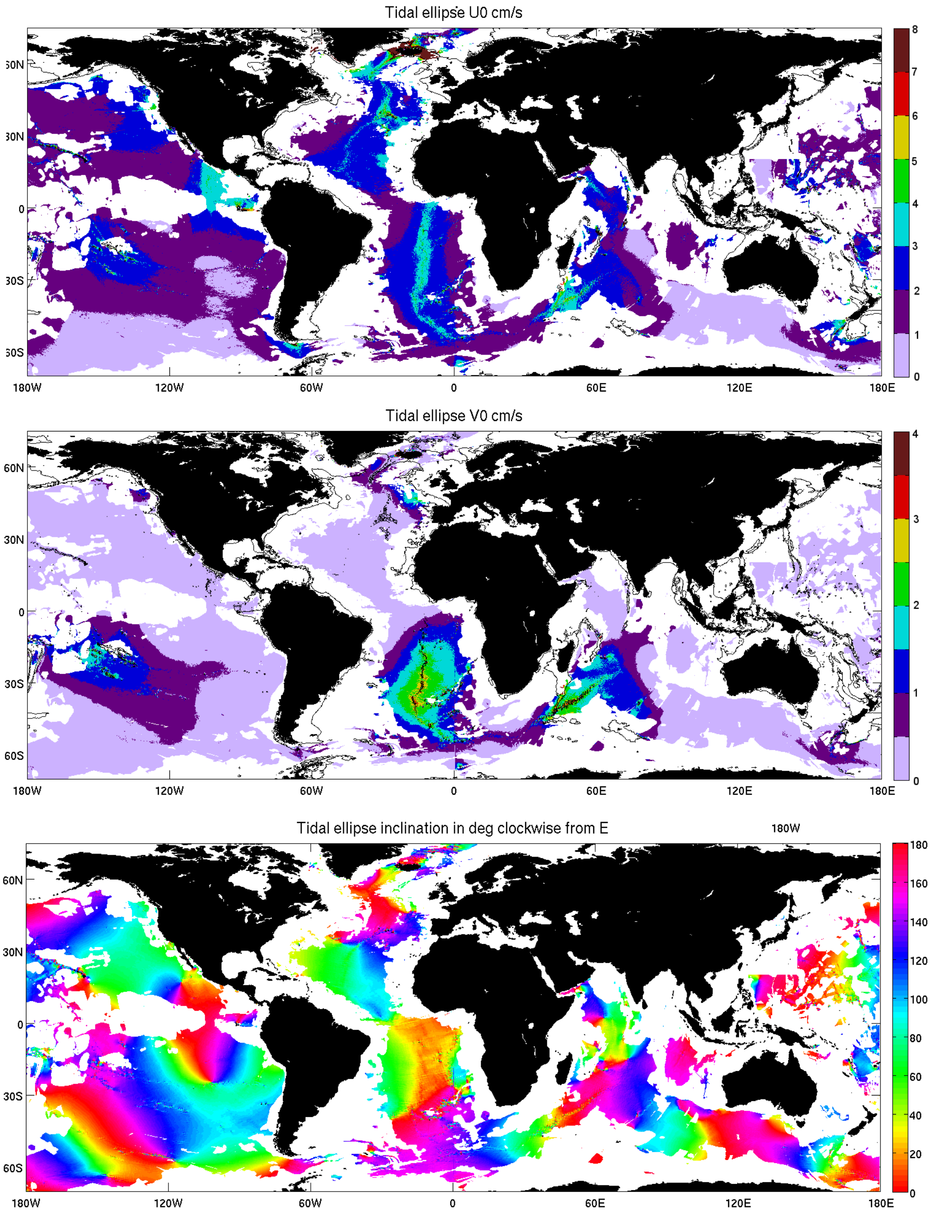

FIG. 3.5: Maps of the M_2 tide parameters U_0, V_0 and α.

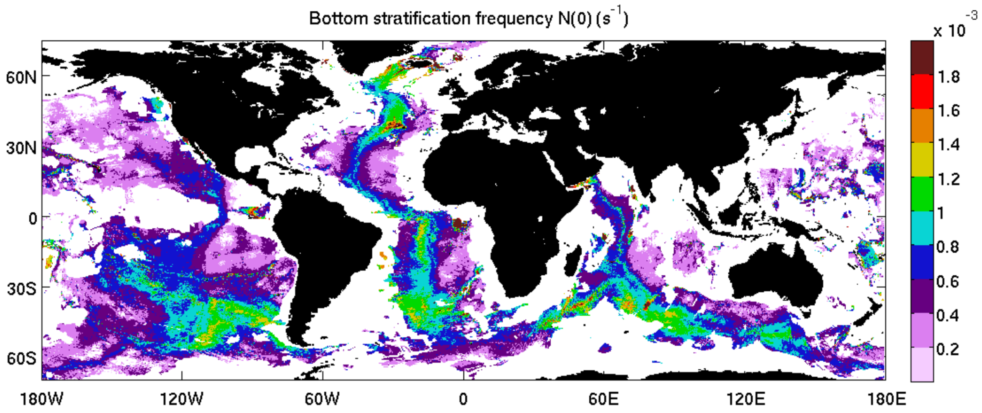

FIG. 3.6: Map of the bottom stratification frequency $N(0)$.

At each location:

- read the P_h parameters $H, k_s, k_n, \theta_s, \nu$, and apply supercritical correction if needed with Eq. (3.3)
- compute corresponding spatial domain length L and resolution dx, and deduce the spectral space (k,l)
- read bottom stratification frequency $N(0)$, Coriolis frequency f, and tidal ellipse ω, U_0, V_0, α
- for each bathymetry sample $1,\ 2,\ \dots,\ N_{\text{sample}}$
  - generate a random and independent sample bathymetry by Eq. (3.1).
  - compute bottom wave amplitude $\hat{A}(k,l,0)$ and energy flux $E(0)$ by linear generation theory using respectively Eq. (2.30) and Eq. (2.34). Apply capping on $\hat{A}$ if needed with Eq. (3.6).
  - determine the most energetic length scale L_A present in $\hat{A}(0)$ by Eq. (3.4), and deduce the saturation length for this sample L_{sat} with Eq. (3.5)
  - at each altitude $z = 0,\ dz,\ 2dz, \dots$ until surface or reflection level $N(z) = \omega_0$
    - ∗ saturate $\hat{A}(k,l,z)$ as follows
      - · Fourier inverse $\hat{A}$ to switch to the real space wave field $A(x,y,z)$
      - · compute where and how much saturation is needed $A_\chi = A(1-1/|A|)\chi_{|A|>1}$ in real space and Fourier transform it $\hat{A}_\chi$
      - · deduce saturated amplitude $\hat{A}_s(z) = \hat{A}(z) - \hat{A}_\chi \times [\kappa^2/(\kappa^2 + L_{\text{sat}}^{-2})]$.
    - ∗ compute $E_s(z)$ by the modified version of Eq. (2.33)
    - ∗ propagate the (now stable) amplitude $\hat{A}_s(z)$ upwards by WKB theory Eq. (2.40) and get $\hat{A}(z+dz)$ (not saturated yet at this altitude)
- compute mean value for $E(0)$ and $E_s(z)$ over all samples.

Chapter 4

Results: the worldwide, three-dimensional structure of tidal dissipation

4.1 Quantities of interest and simulation parameters

The impact of internal-tide-driven mixing is currently parametrized in most climate models by an ad hoc formula for the dissipation rate

$$\varepsilon = \frac{qE_0(x,y)}{\rho}F(z) \tag{4.1}$$

where (x,y) denotes the horizontal longitude-latitude coordinates, z height above bottom and $E_0(x,y)$ the bottom ($z=0$) upward energy flux converted by the waves [denoted $E(0)$ in the previous chapter]. q is the fraction of bottom energy E_0 energy dissipated locally in the whole water column. The dissipation follows the vertical distribution F, which is normalized so that $\int_0^H F(z)\,\mathrm{d}z = 1$ [H is the local ocean depth, or the maximum height above the floor such that $N(z) > \omega_0$]. Recalling the definition of ε Eq. (2.42), the local energy dissipation is simply

$$qE_0 = E_0 - E_s(H) = \rho \int_0^H \varepsilon\,\mathrm{d}z, \tag{4.2}$$

Currently, most climate models use the uniform value $q = 30$ %, based on very few regional estimates. However, the spatial distribution of diapycnal mixing (and hence of q) has been shown to play an important role in the ocean circulation, including the strength of the Antarctic Circumpolar Current [24]. The vertical profile $F(z)$ [divided by $N^2(z)$] is modeled as a exponential decaying with height $F/N^2 \propto \exp(-z/z_0)$, with a fixed and uniform decay scale z_0 (typically $300-500$ m) [25]. Power law decay (with power 2) has also been proposed [26]. Comparing exponential and power law distributions, Melet et al. [27] demonstrated that the long-time ocean state was not only sensitive to the strength of diapycnal mixing, but also to $F(z)$. Our goal is to provide worldwide estimates of the local energy dissipation $q(x,y)$ and its vertical distribution $F(x,y,z)$ to better understand and parametrize where tidal energy is dissipated.

In the following sections, results are averaged over $N_{\text{sample}} = 10$ bathymetry samples. The domain size spatial resolution of each sample is deduced from the two lengthscales provided by the local Goff & Arbic power spectrum P_h (k_n^{-1} and k_s^{-1}). As our code makes intensive use of Fourier transforms, a domain size $N \times N = 2^n \times 2^n$

dz	A_{sat}	L_{sat}	E_0^{cap}
50 m	1.0	$3L_A$	0.1 W m^{-2}

TAB. 4.1: Simulation parameters used in our reference computations [see Eq. (3.4) for L_A]. Number of random samples, domain size and resolution are dealt with in the text.

is desirable. Recalling the preliminary remarks in Chapter 3, and in particular that our results are more sensitive to the value of dx, we first assign

$$dx = \frac{1}{60} \times \frac{2\pi}{k_n}, \tag{4.3}$$

and require at the same time

$$L > 1 \times \frac{2\pi}{k_s}. \tag{4.4}$$

We deduce the smallest power n satisfying these conditions and the corresponding $L = (2^n - 1)\ dx$. In our computation about half of the locations require $N = 256$ and half $N = 512$, and in average, we find that $L \sim 1.5 \times (2\pi/k_s)$. Typical orders of magnitudes are $L = O(25-50)$ km and $dz = O(0.1-0.2)$ km. The remaining simulation parameters are found in Tab. 4.1. The sensitivity of our results with respect to all of the mentioned parameters is investigated in Appendix A.

With our $1/4^\circ \times 1/4^\circ$ longitude-latitude grid resolution, the bottom generation was carried out at $\approx 253{,}000$ locations. To accelerate computations, the vertical propagation and dissipation was only carried out for non-negligible energies $E_0 > 10^{-5}$ W m^{-2}, representing $\approx 176{,}000$ points. With these parameters, each global computation required about a week on a 16 core workstation. In Appendix A we summarize the results of 12 such computations.

4.2 Bottom energy conversion

Our first result is the local bottom energy flux E_0, converted by the waves from the M_2 tide, see Fig. 4.1. Regions of high barotropic energy conversion are found to concentrate around mid-ocean ridges, where the hills are tallest and roughest. The conversion integrates to 104.6 GW globally (standard deviation among 10 samples is < 0.1 GW). These results are consistent with an earlier estimate of 0.1 TW, obtained in spectral space [28]. It is indeed possible to estimate the expected energy flux directly from the power spectrum, replacing $|h|^2(k,l)$ in Eq. (2.34) by $\mathbb{E}[|h|^2(k,l)] = P_h(k,l)$. Doing so, we can check that our empirical mean flux E_0 (computed with 10 bathymetric samples) indeed approximates very well the expected theoretical value E_0^{theory}, see Fig. 4.2. We see that very little deviation occurs, which is confirmed by the expected integral value $E_0^{\text{theory}} = 104.1$ GW. Slightly lighter regions may however be noticed, corresponding to closer approximation. These regions are found to coincide exactly with regions where the domain of samples is larger ($N = 512$ versus $N = 256$). This is not surprising, as integrating the over larger domains (say $L = 50$ km instead of 25 km) artificially corresponds to averaging results over more samples (say 40 instead of 10, since distant locations in space are practically independent from a statistical point of view (decay of the power spectrum implies finite correlation lengths).

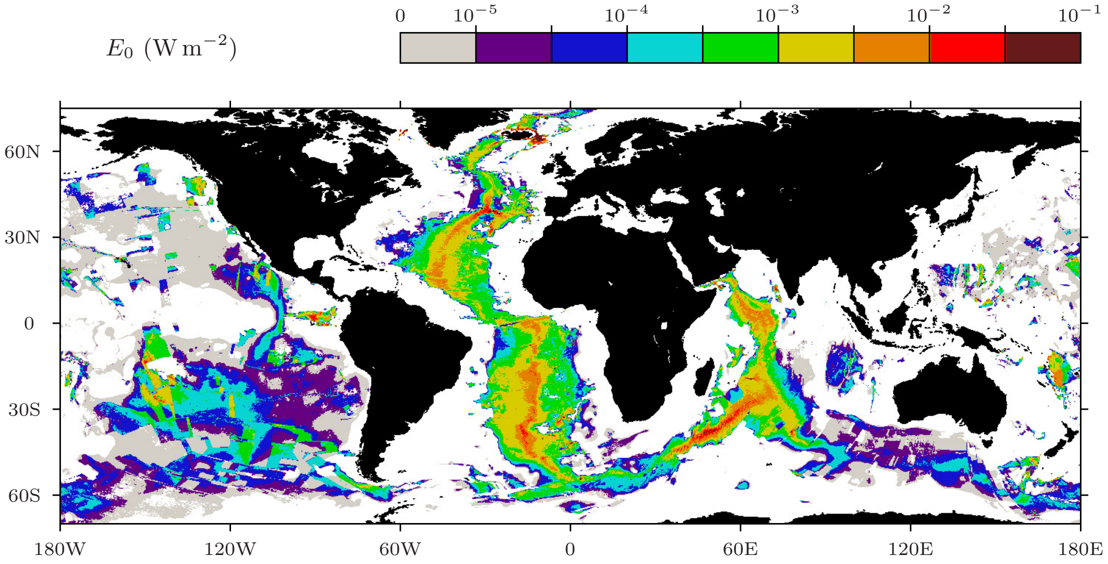

FIG. 4.1: Bottom energy conversion E_0 into internal tides. White regions have no abyssal hills. Grey regions have $E_0 < 10^{-5}$ W m^{-2} and are thus not taken into account in the subsequent computations. Note that the maximum value on the log scale is our capping E_0^{cap}. All data is at 1/4° × 1/4° resolution.

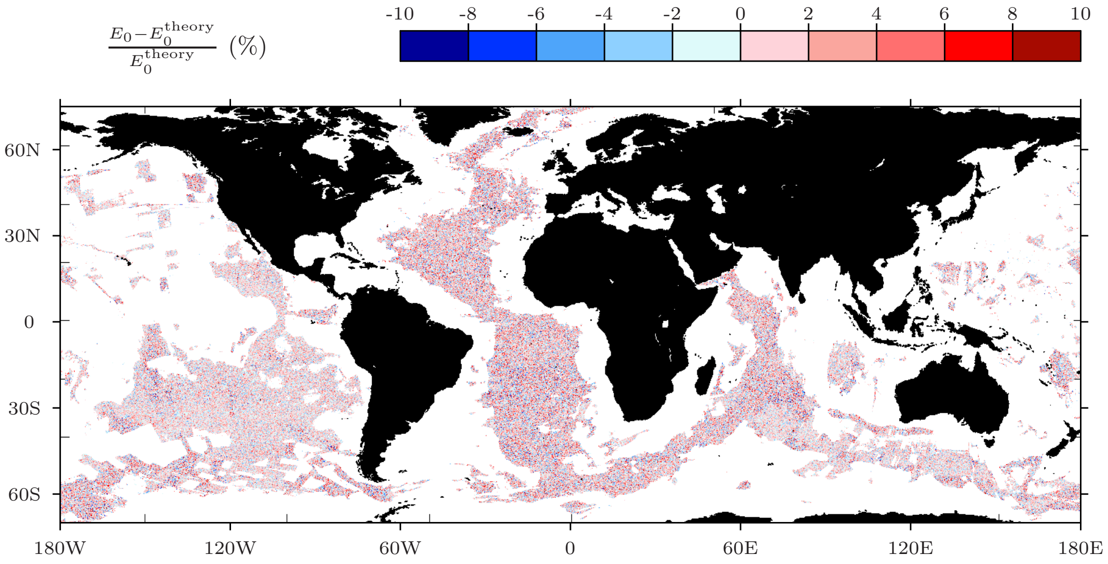

FIG. 4.2: Relative estimation error of the bottom conversion. We compare the empirical flux with the expected value and see excellent agreement.

To conclude this section, we briefly mention the influence of the supercritical correction described in the previous. As shown in Fig. 4.3, the correction has little influence on the energy flux ($<$ 5 % in most regions). This is expected as the supercritical contributions in the power spectrum that are removed would generate small-scale wave, which do not contribute much to E_0. However, they may impact the dissipation above the floor, which is why we remove them. Globally, $E_0^{\text{theory sup}}$ integrates to 107.5 GW (versus 104.1 GW), that is a difference of 3 %.

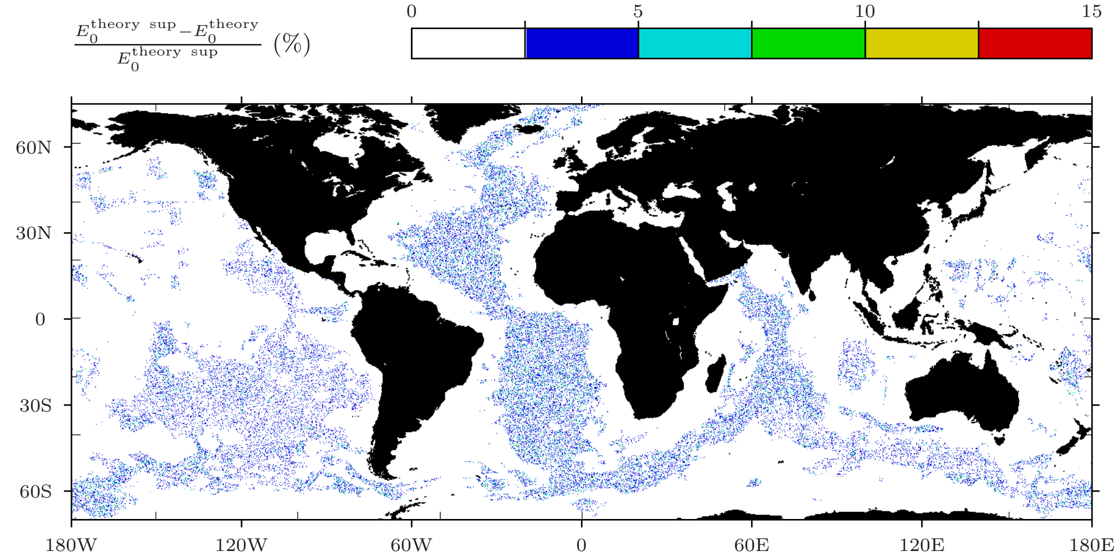

FIG. 4.3: Relative difference between expected supercritical $E_0^{\text{theory sup}}$ and the expected value E_0^{theory} after correction. Since the correction removes a part of the spectrum P_h [see Eq.(3.3)], only positive values are possible.

4.3 Local dissipation fraction

This section is concerned with the truly novel results of the local fraction of tidal dissipation q, shown in Fig. 4.4a. Interestingly, its spatial distribution is far from homogeneous. A few regions exhibit very high values of q, between 60 % and 90 %. Mostly located in the Southern Hemisphere, they include the Mid-Atlantic Ridge, Central Indian Ridge, East Pacific Rise and are surrounded by regions where q decays to $30-60$ %. The dissipation in most of the rest of the deep ocean is found to be below 10 %. The global energy dissipation amounts to 64.1 GW, that is 61 % of the barotropic conversion and about 75 % ($\approx$ 45 GW) is dissipated at hotspots where $q > 60$ % (see Fig. 4.5 for the full distribution). Given the central role of the Southern Ocean in ventilating deep water masses [29, 30], the southern location and energetic importance of these hotspots could have important implications for the global oceanic circulation [31].

This estimate only includes waves generated by abyssal hills. To compare our results with in situ observations, we shall include large-scale waves, generated by larger features $O(50-1000)$ km such as canyons and ridges, whose bathymetry is known deterministically by satellite altimetry. The flux associated to these waves has been computed worldwide recently by Melet et al. [28] and integrates to 875 GW using our capping $E_0^{\text{cap}} = 0.1$ W m^{-1}. For simplicity, since we only compute energy dissipation associated to small-scale abyssal hills, we must assume that *these large-scale waves do not dissipate energy*. This assumption is however supported by recent observations [11] indicating that tidal dissipation is essentially done by the small-scale waves we consider in detail. Motivated by this finding, we investigate and estimate the total fraction including the large-scale energy flux as

$$q^{\text{total}} = \frac{\text{dissipation by small scales}}{\text{energy of small + large scales}} = \frac{qE_0}{E_0 + E_0^{\text{large scale}}}. \tag{4.5}$$

The results are shown in Fig. 4.4b. The same hotspots emerge, albeit with lower magnitudes ($20-60$ %) and more patchiness, reflecting the patchiness of the large-scale energy flux (see Fig. 8a in [28]). The spatial inhomo-

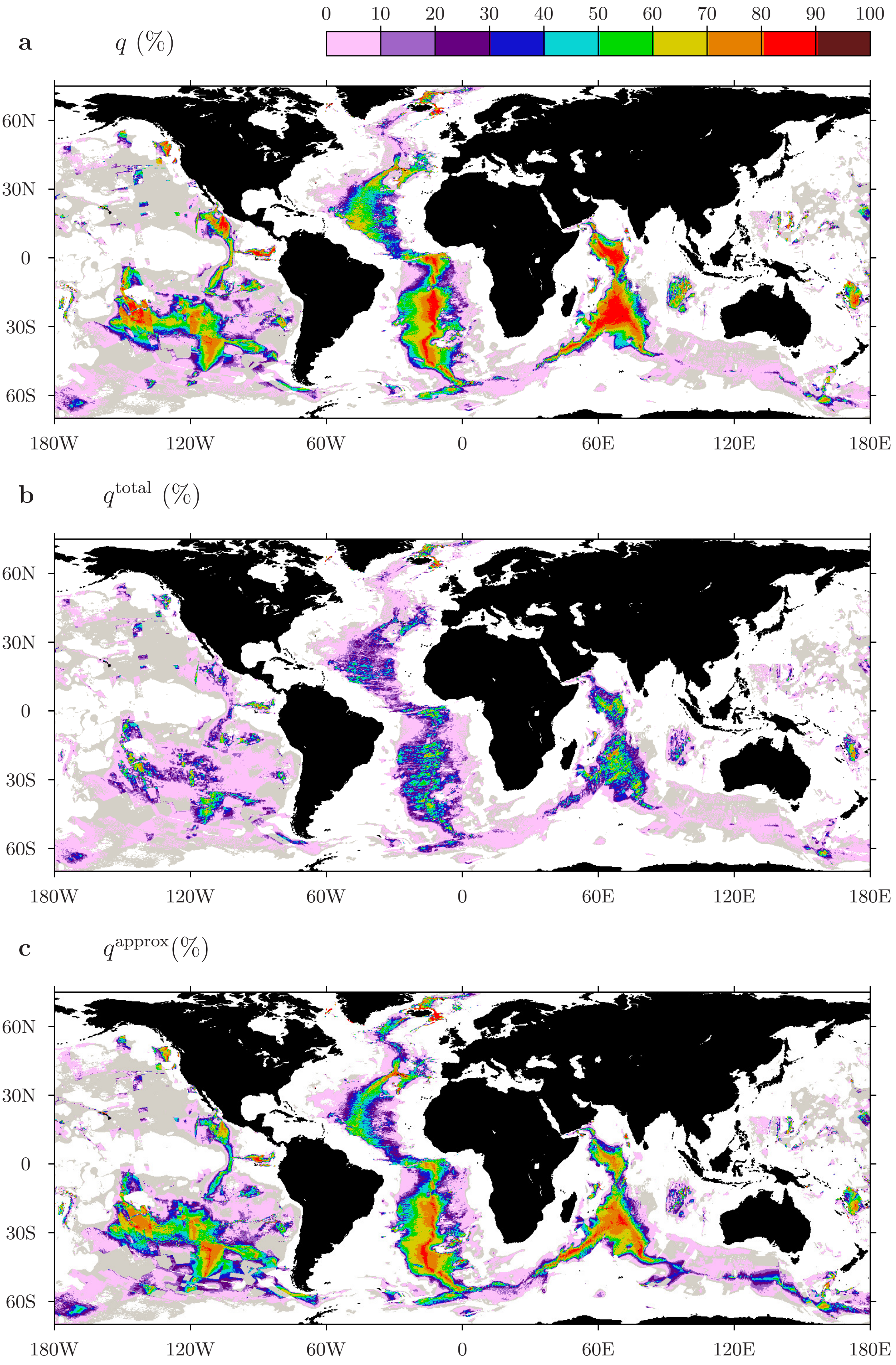

FIG. 4.4: Local dissipation fraction (a) q due to abyssal hills only [see Eq. (4.1)] (b) q^{total} including conversion $E_0^{\text{large scale}}$ by large-scale bathymetry [see Eq. (4.5)] and (c) q^{approx} approximated by bottom rms amplitude A_0^{rms} fitting the data [see Eq. (4.7)]. All data is at 1/4° × 1/4° resolution.

geneity and values of q^{total} are consistent with regional observations [11, 34, 35]. Since abyssal hills contribute to about 10 % to the global conversion [$105 \approx 10\% \times (105+875)$], the global average fraction drops to 6 %, or 17 % restricting the computation to the regions having some small-scale dissipation (not in grey or white).

As expected, we find that q is not only sensitive to the bathymetry, but also to tidal amplitudes and stratification. We find that this dependence may be reasonably well understood by a simple empirical formula q^{approx} based on an instability measure of the waves generated at the bottom. This measure is simply the standard deviation of the bottom amplitude (taken as a random variable) $\sqrt{\mathbb{E}[|A(z=0)|^2]}$ [its mean is of course $\mathbb{E}[A(z=0)] = 0$]. In the following, we call this value the rms amplitude A_0^{rms}. Using our linear theory, it may directly be obtained in spectral space from the local bathymetry Goff & Arbic spectrum and forcing conditions

$$A_0^{\text{rms}} = \sqrt{4\frac{N^2(0)-\omega^2}{\omega^2-f^2}\frac{1}{(2\pi)^2}\iint P_h(k,l)J_1^2\Big(\frac{\sqrt{U_0^2K^2+V_0^2L^2}}{\omega}\Big)(k^2+l^2)\,dk\,dl} \tag{4.6}$$

We emphasize that this formula simply makes use of the *linear theory* and of the abyssal hill and forcing data *at the bottom*. We show that it may be used to predict with surprisingly good accuracy the dissipation fraction q in the whole water column, although this value is conditioned by strongly nonlinear processes. We propose the following expression:

$$q^{\text{approx}} = \begin{cases} 87\Big[1-\exp\Big(-4(A_0^{\text{rms}}-0.1)\Big)\Big] & \text{if} \quad A_0^{\text{rms}} > 0.1 \\ 0 & \text{otherwise.} \end{cases} \tag{4.7}$$

As demonstrated by Fig. 4.4c, this expression captures the spatial distribution of q. We also check that it reproduces well the total dissipation (65.1 GW instead of 64.1 GW). However, this is not the way the approximation Eq. (4.7) is inferred, as we explain next. We start by considering the distribution of q with respect to A_0^{rms} in terms of median curve and two extreme percentiles (10 % and 90 %), see Fig. 4.5a. The approximation is shown to reproduce the median with excellent accuracy. In the meantime, we consider the density of the dissipated energy qE_0 with respect to q (analogue of a probability density function, PDF), see Fig. 4.5b. Integrating this PDF between q_1 and q_2 yields the dissipation by regions with $q_1 < q < q_2$ (integral between 0 and 100 % yields 64.1 GW). Our expression q^{approx} is designed to agree very well with this density, which means that it reproduces very faithfully the energetic contribution of each type of region. Note that the peak near $q = 87$ % is an artifact due to the exponential in our expression. Eventually, Fig. 4.5c shows the primitive of this function (cumulative distribution function, or CDF). As a direct consequence of the previous requirement, excellent agreement is found, confirming the energetic relevance of our approximation.

4.4 Existence of two generic vertical dissipation profiles

We now turn to the vertical structure of tidal dissipation F. As previously explained, we computed vertical profiles at about 176,000 locations (the criterion being $E_0 \geq 10^{-5}$ W m^{-2}). To focus on the truly relevant profiles, we only carry out the following analysis on those satisfying $qE_0 \geq 10^{-5}$ W m^{-2}, that is $\approx 93{,}000$ locations. Acknowledging the amount of information that it represents, we shall try to get generic profiles. For this purpose, we want to remove the influence of the varying stratification frequency $N(z)$ by stretching the

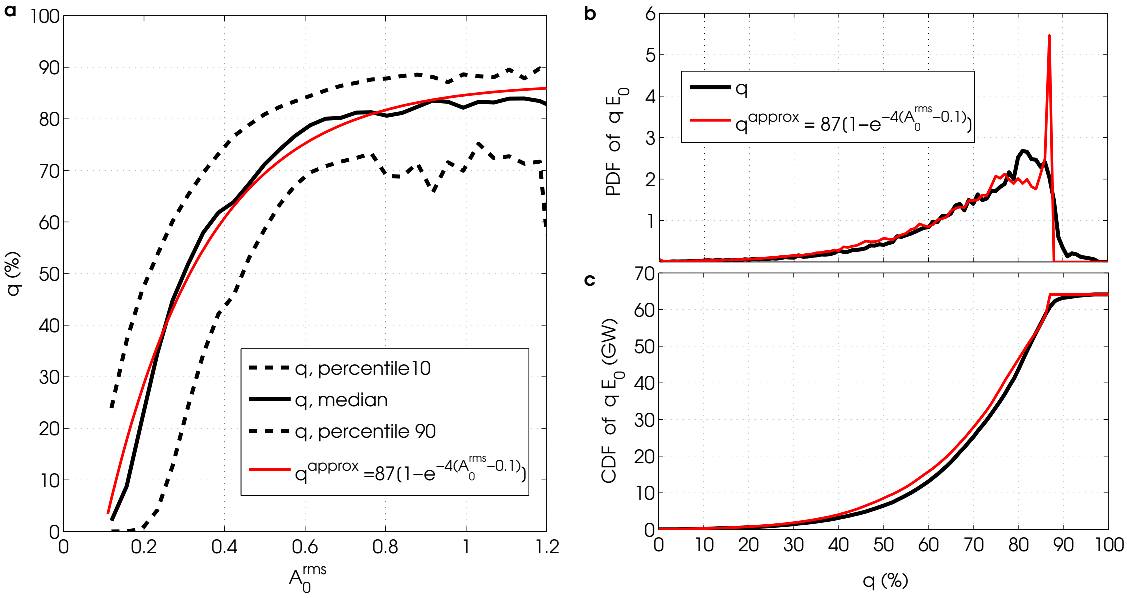

FIG. 4.5: Determination and validity of q^{approx}. (a) Distribution of the empirical and approximated q with respect to A_0^{rms}. (b) Probability density function (PDF) and (c) Cumulative distribution function (CDF) of the dissipation qE_0 with respect to q. Total dissipation amounts to 64.1 GW.

vertical coordinate z using WKB theory [32]

$$z^* = \frac{\int_0^z \sqrt{\frac{N^2(z')-\omega^2}{\omega^2-f^2}}\ \mathrm{d}z'}{\frac{1}{H}\int_0^H \sqrt{\frac{N^2(z')-\omega^2}{\omega^2-f^2}}\ \mathrm{d}z'}. \tag{4.8}$$

As this stretching was not sufficient to collapse $F(z^*)$ profiles, we rescale F by a power of N. The scaling F/N^2 proves to be the best to collapse profiles, thus to ease comparison with the literature, we present results for the diapycnal diffusivity K_ρ, which we presented earlier. Note that global models do not typically use this (intuitive) diffusivity directly to parametrize mixing. We choose to detail our results not in terms of F/N^2 but in terms of $K_\rho = \Gamma\varepsilon/N^2 = (\Gamma q E_0/\rho) \times (F/N^2)$ for the sake of comparison with values found in the literature. However, F profiles may readily be computed back from our K_ρ, q and E_0 data.

To characterize the profiles obtained, we carry a linear regression of $\log(K_\rho)$ in the z^* and $\log(z^*)$ spaces. Though both exponential and power law decay have been suggested for K_ρ (as explained at the beginning of this chapter), we find that the fit is better in the exponential case. However, not all the points obey this exponential decay. Fitting a profile $K_\rho(z^*) = K_\rho(0)\,\mathrm{e}^{-z^*/z_0^*}$, we consider that $z_0^* > 0$ and a coefficient of determination $R^2 > 0.6$ convincingly fit an exponentially decaying profile while the remaining locations correspond to a different profile. According to this criterion, exponentially decaying profiles are found in 25 % of the area covered by dissipation and are responsible for 68 % of the dissipated energy. The remaining profiles, covering the remaining 75 % and dissipating 32 % of the energy, have in common to be non-monotonic and many possess a mid-level 'hump', hence the subsequent name *hump profile*. We shall now describe four typical example profiles.

Fig. 4.6a is a profile typical of regions of high E_0 and q (here, near the Central Indian Ridge, 49°E 38°S). The bottom diffusivity is large $O(10^{-3}\ \mathrm{m}^2\ \mathrm{s}^{-1})$ and the exponential fit is excellent ($R^2 = 0.94$). Note the exponential

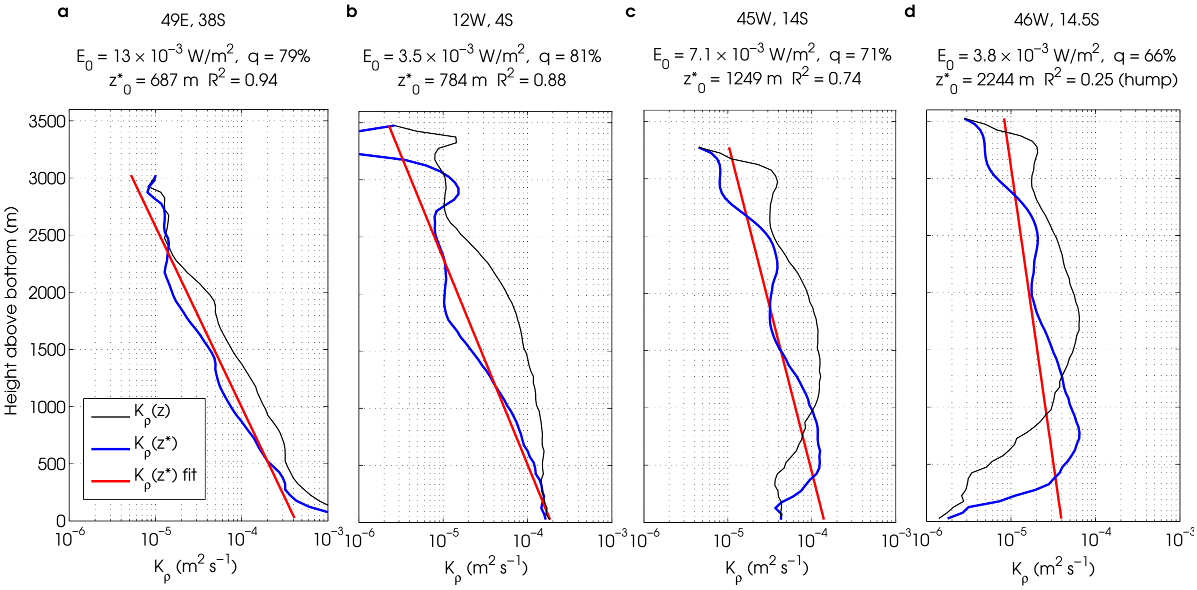

FIG. 4.6: Three typical exponentially decaying profiles, with (a) excellent, (b) good and (c) correct fit. (d) Hump profile, with poor exponential fit $R^2 = 0.25 < 0.6$. Note the difference between $K_\rho(z)$ and $K_\rho(z^*)$.

behavior in both coordinate systems z and z^*. By contrast, Fig. 4.6b shows that in regions of weaker E_0 [and hence weaker $K_\rho(0)$, here $O(10^{-4})$ m^2 s^{-1}] only $K_\rho(z^*)$ is reasonably exponential. The fit is still very good in average, with $R^2 = 0.88$. Figure Fig. 4.6c portrays an even weaker profile, still decaying with height and exponential in average but resembling more and more a hump profile. The decay scale is larger and the fit of lesser quality ($R^2 = 0.74$). This profile is typically found over the smoother ridge flanks (here by the Mid-Atlantic Ridge). As explained, we consider that the profile is a hump profile if $R^2 < 0.6$,. This profile type transition is illustrated in Fig. 4.6d ($R^2 = 0.25$), which is located very close to the previous point (46°W 14.5°S versus 45°W 14°S). Note the difference between the altitude of the maximum K_ρ (hump) in the two coordinate systems. Though we do not provide evidence for the sake of brevity, we find that using the z^* coordinate the only way to efficiently collapse most hump profiles, as we shall discuss later.

The bottom-heavy diffusivity of exponential profiles is due to high bottom wave amplitudes, more likely to be unstable close to their generation site. Hump profiles by contrast exhibit stronger diffusivity higher up in the water column due to increased ambient stratification, yielding smaller-scale waves of larger amplitudes. We therefore expect exponential profiles to dominate when the bottom amplitudes are large and vice versa. This is confirmed by Fig. 4.7a, showing the distribution of the dissipated energy with respect to the rms amplitude A_0^{rms}. The two profiles may indeed be diagnosed *a priori* according to the bathymetry and forcing conditions at the bottom: if $A^{\mathrm{rms}}(0) > 0.4$, the diffusivity decays exponentially and vice versa.

4.5 Exponentially decaying diffusivity profiles

The analysis of a few percentiles of the whole distribution of $\approx 24{,}000$ exponential profiles is shown in figure Fig. 4.7c. The most energetic profiles indeed follow almost perfect exponential decay, and we shall later show

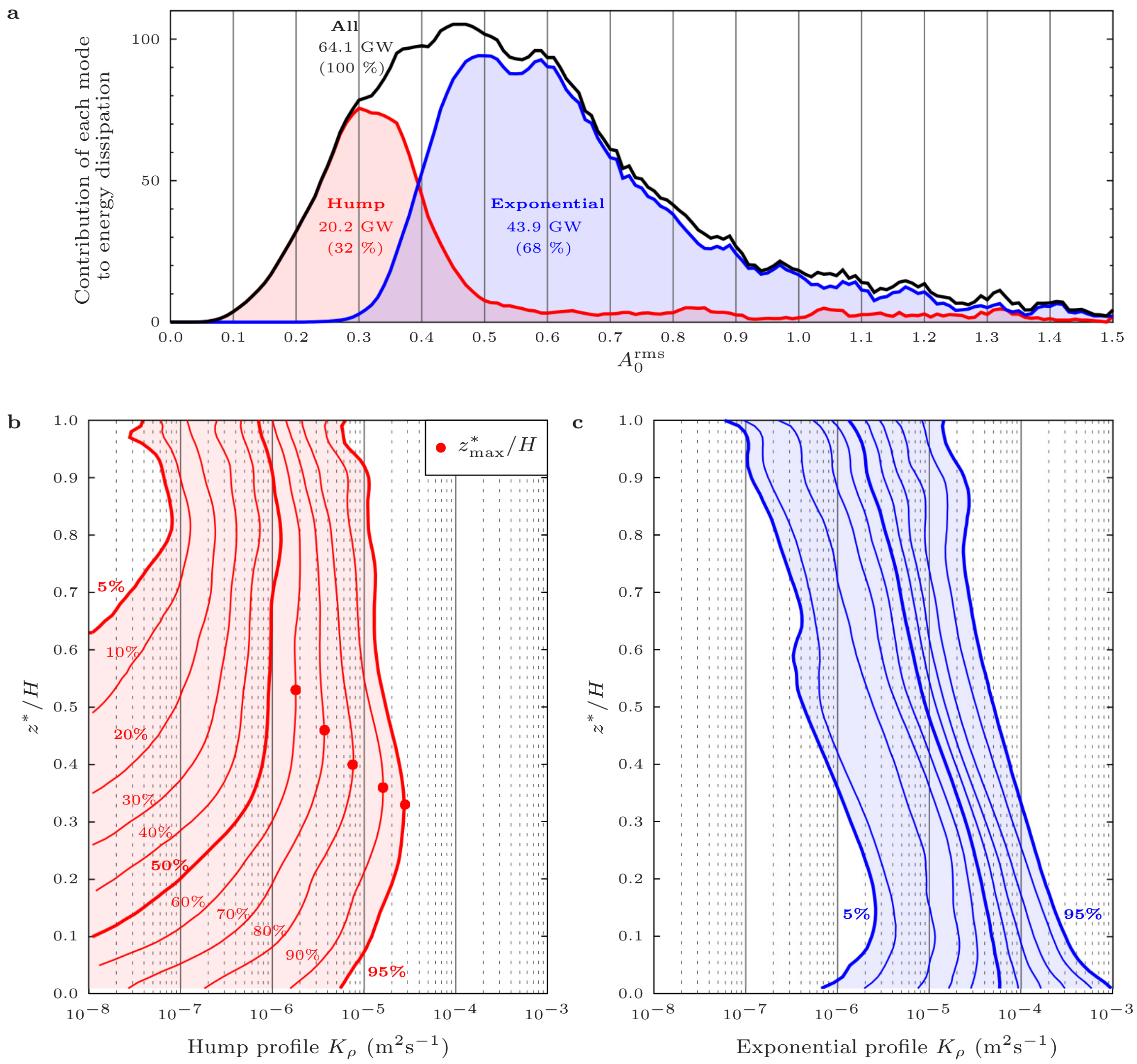

FIG. 4.7: Existence of two vertical profiles of dissipation. (a) Density of the dissipated energy with respect to the linear bottom amplitude A_0^{rms} and contribution of each profile. Integral yields 64.1 GW. Exponential and hump profiles are clearly separated by the value $A_0^{\mathrm{rms}}(0) = 0.4$. (b) Percentiles of the $\approx 69{,}000$ hump profiles of K_ρ. Note the transition from mid-level maxima (most energetic percentiles) to profiles with no bottom mixing and constant upper-level mixing. (c) Percentile of the $\approx 24{,}000$ exponential profiles of K_ρ [same percentile values as in (b)].

that indeed half of the energy is dissipated by exponential profiles having $R^2 > 0.9$. At these locations, K_ρ typically reaches $10^{-4} - 10^{-3}$ m^2 s^{-1}, in consistentcy with in situ observations above rough bathymetry [2, 33, 34]. Lower percentiles, though still exponential in average, continuously deform and end up akin to a hump profile.

The map of the exponential decay scale z_0^* is reported in Fig. 4.8a. Exponential profiles (brown to blue) clearly coincide with regions of high dissipation (hotspots of q). This is expected since exponential decay corresponds to large bottom amplitudes ($A_0^{\mathrm{rms}} > 0.4$, see Fig. 4.7a, and hence, from Eq. (4.7), to large values of q ($q > 87[1 - \mathrm{e}^{-4(0.4-0.1)}] \sim 60$ %). The decay scale is typically smaller than 1000 m (80 % of the dissipation), with regions atop the ridges exhibiting the fastest decays (250 – 750 m). (Anticipating our figures, the full distribution may be seen in Fig. 4.9.) Regions near Iceland feature $z_0^* < 250$ m, though very large amplitudes due

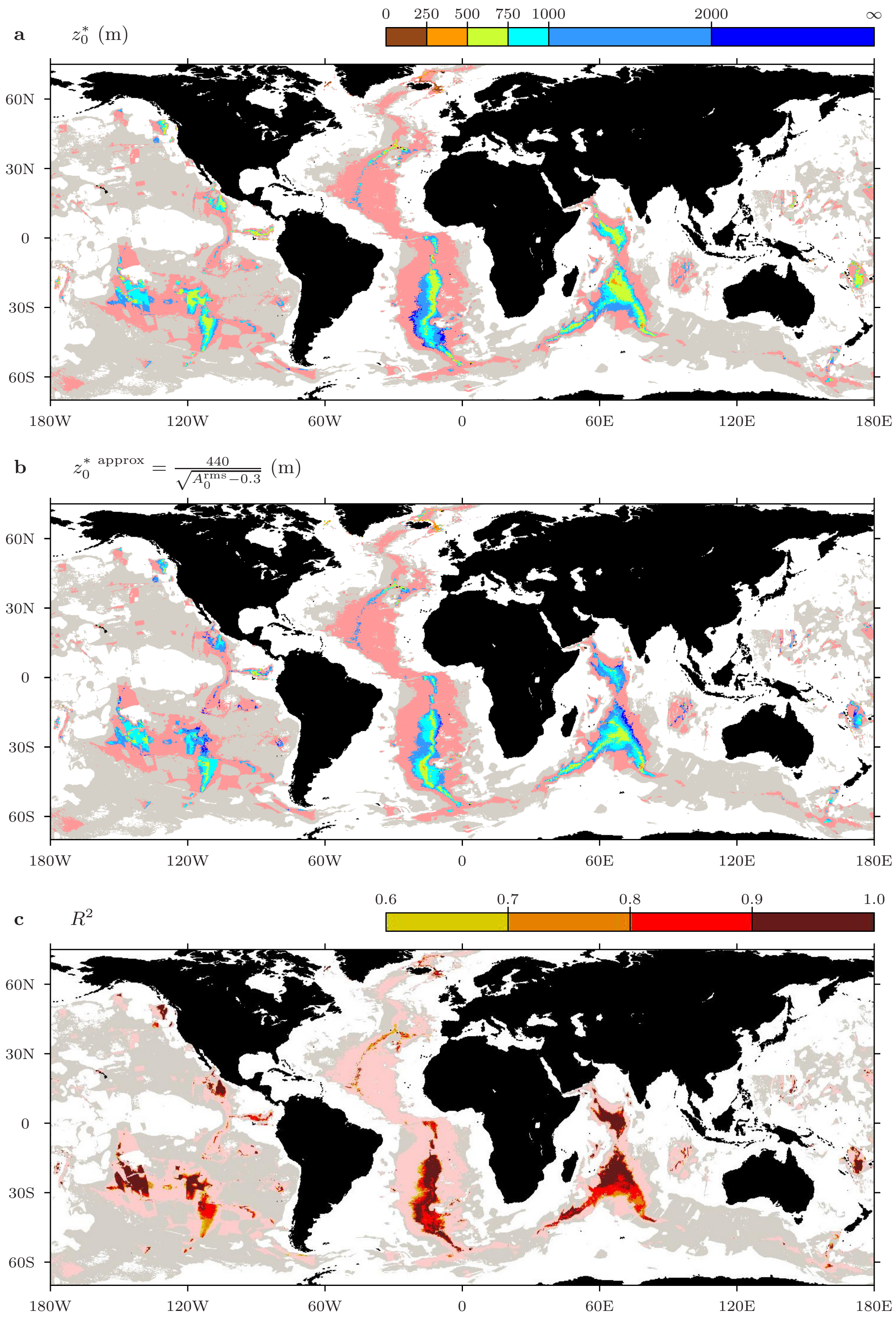

FIG. 4.8: (a) Decay scale of exponential profiles z_0^* determined by the linear regression on real exponential profiles of $\log(K_\rho)$ with WKB-scaled z^* coordinate. (b) $z_0^{*\,\mathrm{approx}}$ predicted by the bottom amplitude $A^{\mathrm{rms}}(0)$ and fitting the data, see Eq. 4.9. (c) Regression parameter R^2. White stands for no abyssal hills as in Fig. 4.1. Grey now indicates too little barotropic conversion *or* dissipation $qE_0 < 10^{-5}$ W m^{-2}. Pink stands for regions of hump profiles.

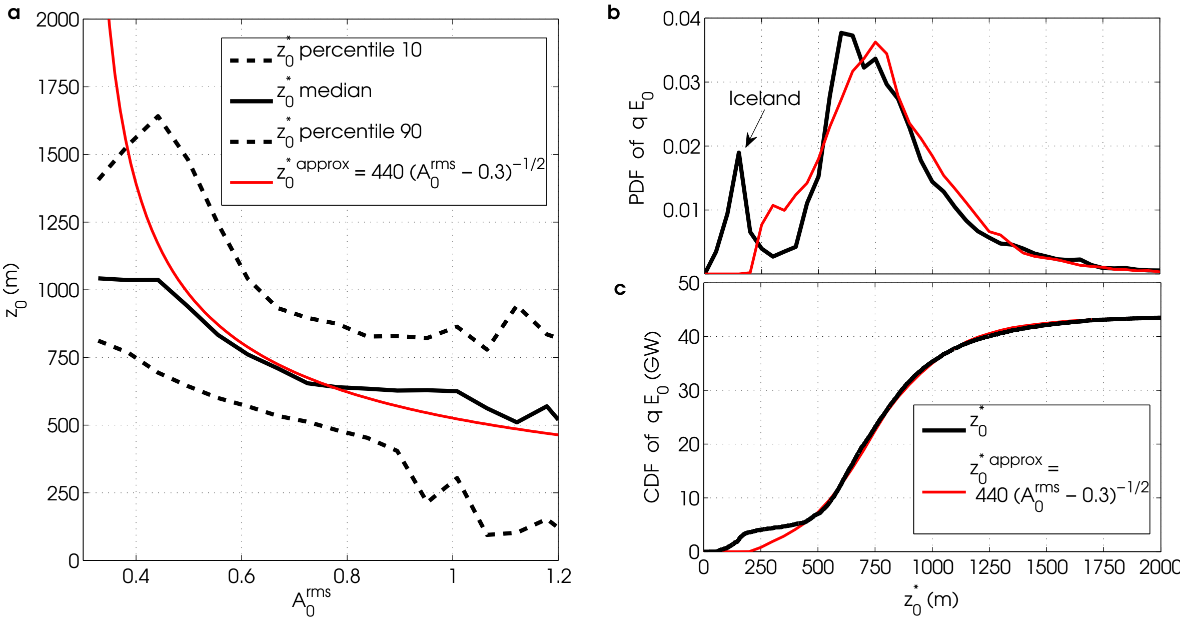

FIG. 4.9: Determination and validity of $z_0^{*\text{approx}}$. (a) Distribution of the empirical and approximated z_0^* with respect to A_0^{rms}. (b) Probability density function (PDF) and (c) cumulative distribution function (CDF) of the dissipation qE_0 with respect to z_0^*. Total amounts to 44 GW (energy dissipated by exponentially decaying profiles).

to poor tidal data gives us little confidence in these results. The map giving the corresponding R^2 value is shown in Fig. 4.8c. As anticipated from the analysis of percentiles, the most energetic regions feature very high values $R^2 > 0.9$, while lower values $0.6 < R^2 < 0.8$ are extremely rare. Note that the decay scale z_0^* is an e-folding value in the WKB-scaled vertical height z^*, *not* in z. Profiles in the z coordinate are found to correlate more weakly with exponential decay (lower R^2 values).

As was the case for q, the spatial distribution $z_0^*(x,y)$ can also be reasonably well understood from the amplitude $A_0^{\text{rms}}(x,y)$. Physically, larger bottom amplitudes yield faster decay, and we indeed find that $(1/z_0^*)^2$ scales quasi-linearly with A_0^{rms}. We propose the approximation

$$z_0^{*\ \text{approx}} = \frac{440}{\sqrt{A_0^{\text{rms}} - 0.3}}, \qquad \text{valid for} \qquad A_0^{\text{rms}} \geq 0.3. \tag{4.9}$$

Fig. 4.8b shows that this expression recovers most of the salient features observed in Fig. 4.8a. However, as we explained for q^{approx}, spatial agreement was not looked after when inferring Eq. (4.9). We inferred it according to the method detailed previously. Fig. 4.9a shows that our approximation reproduces well the median distribution of decay scales 500 m $< z_0^* <$ 1000 m. We note that the expression $z_0^{*\ \text{approx}}$ breaks down for $A_0^{\text{rms}} \leq 0.3$, but such values are not representative of the exponential mode anyway as we have seen. Fig. 4.9c confirms that this agreement is excellent in terms of cumulated energy, while the full density is not as well captured (Fig. 4.9b). This is due in part to shallow regions, especially around Iceland, where extreme tidal amplitudes cause $z_0^{*\ \text{approx}} < 250$ m (see arrow). Our opinion is that such values are unreliable and our model is not designed to predict them. A capping of $E_0^{\text{cap}} = 1$ W m^{-2} (instead of $E_0^{\text{cap}} = 0.1$ W m^{-2} here) would evidently amplify this peak.

4.6 Hump diffusivity profiles

The analysis of the percentiles of $\approx 69,000$ hump profiles in Fig. 4.7b reveals that the most energetic ones $80-95$ exhibit a prominent *mid-depth diffusivity maximum* at $z^*_{max}/H \sim 0.3-0.5$, which can be larger than the oceanic background value 10^{-5} m^2 s^{-1}. It comes from a dramatic increase in dissipation ε due to larger ambient stratification, not compensated by the WKB and $1/N^2$ scalings. Although the stratification at these locations is not stronger than elsewhere, the gradual increase of $N(z)$ in the abyssal ocean suffices to make these waves, stable at the bottom, break well above the seafloor. Observations do suggest the possibility of non-monotonic diffusivity profiles in certain regions [2, 33]. Our results indicate that those profiles, not accounted for in current mixing parameterizations, cover large regions and are responsible for a significant fraction of the tidal dissipation. Understanding and predicting their characteristics could benefit parametrizations and yield a different ocean circulation than that obtained with classical mixing schemes.

For this purpose, and by analogy of our previous analysis, the height and strength of the mid-depth maximum can be related to A_0^{rms}, see Fig. 4.10. We start by determining the maximum diffusivity $K_\rho(z^*_{\mathrm{max}})$ values as follows. We lists all points that are local maxima in the 300 m neighbourhood above them. We then reject the artificial ones occuring in a 300 m neighbourhood of the global maximum of N (thermocline) and select the one having the greatest K_ρ value. As shown in the percentile distribution, only the most energetic profiles were found to possess such a maximum, and Fig. 4.10 only concerns those profiles. Fig. 4.10a shows that the maximum diffusivity $K_\rho(z^*_{max})$ increases with the bottom amplitude, and its median value exceeds 10^{-5} m^2 s^{-1} for $A_0^{\mathrm{rms}} > 0.35$. Fig. 4.10b shows that the relative height z^*_{max}/H at which the maximum occurs is found to decrease with A_0^{rms}, in consistency with the idea that statistically less stable bottom waves break at lower heights, being more sensitive to the increase of $N(z)$. To refine this analysis further, we look at the would-be amplitude at the height where the maximum occurs $A^{\mathrm{rms}}(z^*_{max})$. According to WKB theory, we write

$$A^{\mathrm{rms}}(z^*_{max}) = A_0^{\mathrm{rms}} \times \left(\frac{N^2(z^*_{max}) - \omega_0^2}{N^2(0) - \omega_0^2} \right)^{1/4}. \tag{4.10}$$

Note that this formula (obtained by linear theory) totally ignores the nonlinear saturation that A undergoes between $z^* = 0$ and $z^* = z^*_{max}$. Nevertheless, Fig. 4.10c demonstrates that the density of energy, not very localized with respect to A_0^{rms}, concentrates around $A^{\mathrm{rms}}(z^*_{max}) = 0.5$. The width of the distribution at half maximum indeed drops by a factor of 2.5. We conclude that $A^{\mathrm{rms}}(z^*_{max}) = 0.5$ may serve as a reasonable criterion to determine *a priori* the height of the diffusivity maximum.

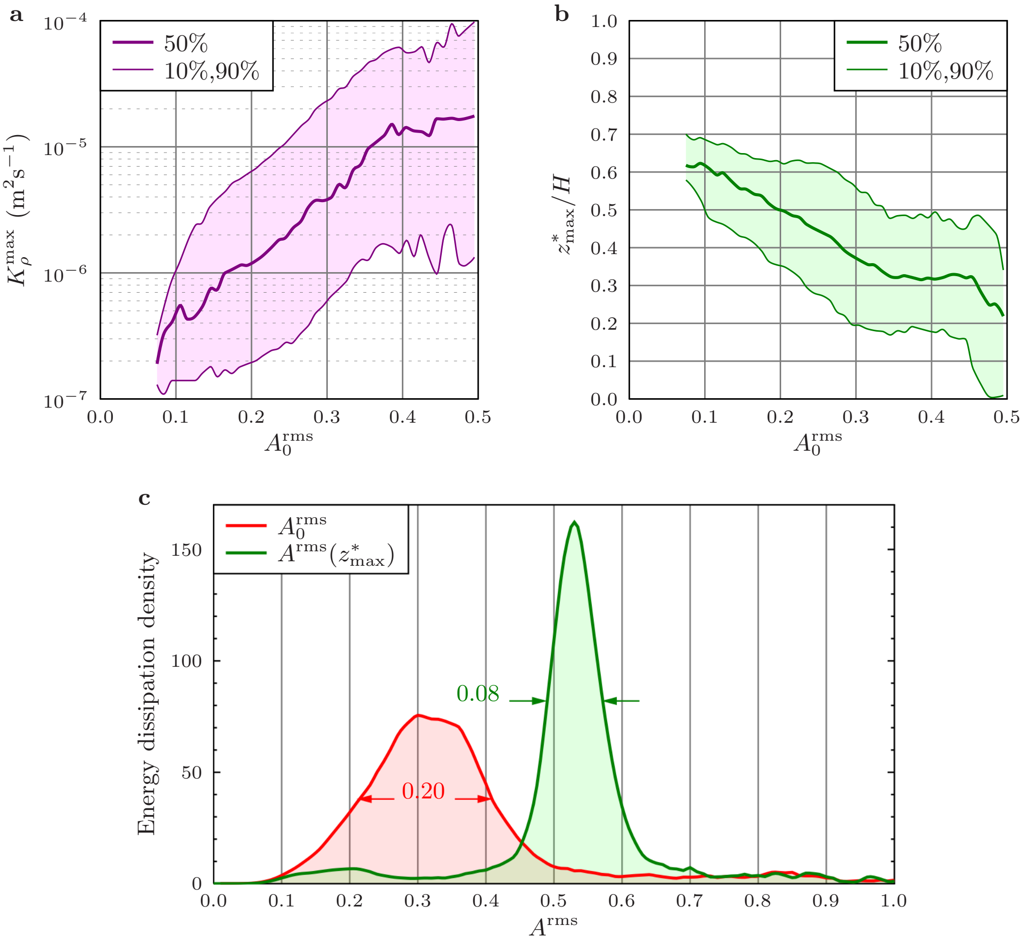

FIG. 4.10: Quantitative characteristics of the hump profiles. (a) Maximum mid-depth diapycnal diffusivity $K_\rho(z^*_{\max})$. Note the increase with the linear measure of bottom wave instability A_0^{rms}. (b) Corresponding relative height z^*_{max}/H . (c) Dissipated energy density versus A^{rms} at $z^* = 0$ and $z^*_{\max}$ as defined in Eq. (4.10) (both integrals yield 20.2 GW). Note how the values of the half-maximum width change, suggesting $A^{\mathrm{rms}}(z^*_{\max}) = 0.5$ to determine $z^*_{\max}$.

Conclusions and directions for future work

In this work, we considered the vertical energy dissipation of internal tides. These internal waves generated by tidal currents are currently believed to provide a large part of the mixing observed in the deep ocean. Our motivation is twofold. On one hand, we aim at a better understanding of where and how a significant part of the available tidal power is dissipated. On the other hand, global climate models need accurate small-scale predictions to parametrize dissipation and simulate accurately the ocean state and its large-scale circulation. We focused on internal tides produced by small-scale abyssal hills, known for their propensity to instability during upward propagation in the bulk of the ocean. Using worldwide numerical computations based on global data for the seawater properties and seafloor topography, we obtained three-dimensional maps of the vertical energy dissipation.

In Chapter 2 we introduced the common approximations of geophysical fluid dynamics, deduced the existence of internal waves by linearizing the Boussinesq model and underlay their most important characteristics. We presented the linear theory for the generation and upward propagation of internal tides in a realistic ocean with inhomogeneous vertical stratification. We then turned to the more puzzling problem of wave instability and turbulent dissipation, and motivated our choice of a simple nonlinear saturation scheme to parametrize wave breaking. After clarifying the physical scales of relevance in our problem, we addressed the challenge of using global data for the ocean seafloor and introduced the statistical description of abyssal hills.

Chapter 3 was devoted to the detailed presentation of our numerical model, and of the points deserving particular attention in its implementation. We have seen how independent random bathymetry samples could be generated from local geological properties, tackled the issue of domain size and grid resolution to ensure its accurate representation and derived an efficient way to interactively set an important saturation parameter. We also explained how we obtained global data for tidal currents and ocean stratification frequency N before writing down our complete algorithm.

In Chapter 4, we saw how current climate models parametrize the turbulent dissipation rate ε, explaining our subsequent focus on the local (depth-integrated) fraction of tidal energy dissipated $q(x,y) \propto \int_0^H \varepsilon \, \mathrm{d}z$ as well as its vertical profile in z. Our computations yielded the bottom energy E_0, converted from the tides by the waves at the seafloor, and we found that it integrates to 105 GW globally. Our first important result was that 61 % of this energy is dissipated, mainly at localized hotspots of very high dissipation $60\% < q < 90\%$ near spreading ridges, where the hills are tallest and roughest. Mainly located in the Southern Hemisphere, these hotspots could impact deep water masses in formation in the Southern Ocean. Including the energy of internal tides generated by larger-scale canyons and ridges, the global fraction dropped to 6 %, yet the same hotspots of q emerged with significant magnitude $20\% < q < 60\%$. We showed that such values compared favorably with available in situ observations. As far as the vertical distribution of ε is concerned, about 70 % of the dissipation followed exponentially decaying profiles for the vertical diffusivity $K_\rho \propto \varepsilon/N^2$, as suggested in the literature. More importantly however, we revealed that the remaining dissipation gave rise to non-monotonic diffusivity (or mixing) profiles, possessing a mid-level maximum. These ”hump profiles”, which we rationalized by variations in ocean stratification with height, are currently not accounted for in parametrizations and could impact the global oceanic circulation. Our third major finding was that the main properties of our three-dimensional map of tidal dissipation may all be surprisingly well understood and predicted by the linear theory. Using a single scalar measure of wave instability at the seafloor, we proposed empirical formulas to approximate q, predict the profile type, approximate the decay scale of exponential profiles and the location of the maximum of hump profiles. Solely depending on seafloor properties, tidal and stratification forcing, our expressions could potentially be used for time-evolving parametrizations in long-term climate models.

Further efforts to complement this work should first concentrate on assessing the respective role of the different types of instabilities that internal tides likely experience. Our nonlinear breaking scheme indeed only implements dissipation due to a static instability, occurring when dense waters are brought on top of lighter ones by large enough wave amplitudes. Yet it is known that internal waves can break and dissipate their energy through other mechanisms, such as shear or subharmonic parametric instabilities [36, 37]. Though understanding and including them in a simple numerical model constitutes a challenge, it may unveil interesting phenomena and amend our conclusions. We also want to emphasize that we solely considered the dissipation of small-scale internal waves generated by abyssal hills. Future work should try to model numerically both small-scale (stochastic) and large-scale (deterministic) waves and investigate their joint behavior and dissipation. This would enable to confirm or infirm the lingering assumption that scale separation prevents the small-scale (unstable) waves to impact the large-scale (stable) waves. As the latter carry close to ten times as much energy as the former, our results indicate that a modest breach in this backbone hypothesis could have serious implications.

Appendix A

Sensitivity analysis and robustness

We start by reporting the sensitivity of our world-integrated results E_0, q and q^{total} to the value of dx in Tab. A.1. The previous condition $dx = (1/60) \times (2\pi/k_n)$ [see Eq. (4.3)] is first relaxed to $dx = (1/30) \times (2\pi/k_n)$, thus effectively dividing all domain sizes N by 2, without changing L. The influence of L may be seen with the next case $dx = (1/40) \times (2\pi/k_n)$, changing both dx and L. We see that E_0 is almost unchanged while q seems to converge from $\approx 50\%$ to $\approx 60\%$ as the resolution is increased. This behavior is not surprising: E_0 in primarily influenced by large-scales but small-scale waves generated by small bathymetric features are more prone to breaking, hence resolving them better enhances dissipation.

The influence of the vertical resolution dz is reported in Tab. A.2. Propagating the waves and saturating their amplitude with smaller increments dz logically increases dissipation. However, to keep computation time reasonable, and not to overestimate dissipation, the value $dz = 50$ m is chosen as reference.

We turn to the influence of slightly more permissive values of saturation threshold A_{sat} in Tab. A.3 and of different saturation lengths L_{sat} in Tab. A.4. For the highest value $A_{\text{sat}} = 1.2$, q is reduced from 61 % to 54 %. Our results also show that the sensitivity to L_{sat} disappears for $3\ L_A \leq L_{\text{sat}} \leq 5\ L_A$, and dissipation is maximized. Hence, the value chosen in Eq. (3.5) ($L_{\text{sat}} = 3\ L_A$) for our reference case seems to yield a robust and physically consistent saturation scheme.

Eventually, as the most (reliable) energetic regions rarely exceed $E_0 = 0.5 \times 10^{-1}$ W m^{-2}, we decided to set $E_0^{\text{cap}} = 10^{-1}$ W m^{-2}. However, calculations with $E_0^{\text{cap}} = 1$ W m^{-2} (as in Melet et al. [28]) are reported in Tab. A.5. They obviously result in a larger global E_0 and in more dissipation ($q = 67$ % versus 61 %). This is due to the fact that very high amplitude waves tend to be highly unstable and dissipate most of their energy.

To conclude, our results are robust with respect to the numerical parameters used, provided that reasonable and physical values are used. The tidal energy conversion by abyssal hills integrates to ≈ 100 GW and its dissipation amounts to $q \approx 55-65$ %. Including large scales, but assuming that they do not dissipate energy, we have $q^{\text{total}} \approx 6-7$ %.

Requirement on dx	**$\frac{1}{60}\times\frac{2\pi}{k_n}$**	$\frac{1}{30}\times\frac{2\pi}{k_n}$	$\frac{1}{40}\times\frac{2\pi}{k_n}$
Deduced N	**512 (55 %), 256 (45 %)**	256 (55%), 128 (45 %)	256 (70%), 128 (30 %)
E_0 (GW)	**104.6**	105.1	105.2
q (%)	**61.3**	49.6	55.8
q^{total} (%)	**6.55**	5.32	5.99

TAB. A.1: Sensitivity of the bottom energy flux E_0, global dissipation fraction q and q^{total} (including the large-scale energy flux $EF_0^{\text{large scale}} = 845$ GW) to domain length L and resolution dx. Reference results presented in Chapter 4 are in bold.

dz (m)	100	**50**	30
q (%)	56.7	**61.3**	63.6
q^{total} (%)	6.06	**6.55**	6.80

TAB. A.2: Sensitivity of q and q^{total} to the vertical step size dz. Reference in bold.

A_{sat}	**1.0**	1.1	1.2
q (%)	**61.3**	57.6	53.9
q^{total} (%)	**6.53**	6.16	5.76

TAB. A.3: Sensitivity of q and q^{total} to the saturation threshold A_{sat}. Reference in bold.

L_{sat}	L_A	2 L_A	**3 L_A**	4 L_A	5 L_A
q (%)	52.2	59.5	**61.3**	61.5	61.2
q^{total} (%)	5.57	6.36	**6.55**	6.58	6.54

TAB. A.4: Sensitivity of q and q^{total} to the saturation length L_{sat} [L_A defined in Eq. (3.4)]. Reference in bold.

E_0^{cap} (W m^{-2})	**0.1**	1
E_0 (GW)	**104.6**	136.2
$E_0^{\text{large scale}}$ (GW)	**875**	1020
q (%)	**61.3**	66.9
q^{total} (%)	**6.55**	7.88

TAB. A.5: Sensitivity of E_0, q and q^{total} to E_0^{cap}. Calculation of $E_0^{\text{large scale}}$ is made in [28]. Reference in bold.

References

[1] Egbert, G. D., & Ray, R. D. Significant dissipation of tidal energy in the deep ocean inferred from satellite altimeter data. *Nature* **405**, 775-778 (2001)

[2] Polzin, K. L., Toole, J. M., Ledwell J. R. & Schmitt, R. W. Spatial variability of turbulent mixing in the abyssal ocean. *Science* **276**, 93-96 (1997).

[3] Vallis G. K. *Atmospheric and oceanic fluid dynamics. Fundamentals and large-scale circulation*. Cambridge University Press (2006).

[4] Caulfield C. P. *Fluid Dynamics of the Environment*. Lecture notes, Ecole polytechnique (2013).

[5] Cushman-Roisin, B. & Beckers J-M. *Introduction to geophysical fluid dynamics. Physical and Numerical Aspects*. Second edition. Academic Press (2011).

[6] Bell, T. H. Lee waves in stratified flows with simple harmonic time dependence. *J. Fluid Mech.*, **67**, 705-722 (1975).

[7] Garrett, C. & Kunze E. Internal tide generation in the deep ocean. *Ann. Rev. Fluid Mech.*, **39**, 57-87 (2007).

[8] Bühler, O. & Muller, C. J. Instability and focusing of internal tides in the deep ocean. *J. Fluid Mech.*, **588**, 1-28 (2007).

[9] Muller, C. J. & Bühler, O. Saturation of the internal tides and induced mixing in the abyssal ocean. *J. Phys. Oceanogr.*, **39**, 2077-2096 (2009).

[10] Muller C., Melet A., & Nikurashin M. Wave saturation: A simple tool to estimate tidal dissipation in the deep ocean. *Geophys. Res. Lett.*, In press (2014).

[11] St. Laurent, L. C. & Nash, J. D. An examination of the radiative and dissipative properties of deep ocean internal tides. *Deep Sea Res. II* **51**, 3029-3042 (2004).

[12] Osborn, T., & C. Cox (1972) Oceanic fine structure. *Geophys. Astrophys. Fluid Dyn.*, **3**, 321-345.

[13] Khatiwala S. Generation of internal tides in an ocean of finite depth: analytical and numerical calculations. *Deep Sea Res. I* **50**, 3-21 (2003).

[14] `http://geology.uprm.edu/MorelockSite/morelockonline/1-summsf.htm` and `http://www.log.furg.br/ocean/wormuth/provinces.html` (visited on 22 July 2014).

[15] Goff, A. J. & Jordan, T. H. Stochastic modeling of seafloor morphology: inversion of sea beam data for second-order statistics. *J. Geophys. Res.*, **93**, 13589-13608 (1988).

[16] Goff, A. J. & Arbic, B. K. Global prediction of abyssal hill roughness statistics for use in ocean models from digital maps of paleo-spreading rate, paleo-ridge orientation, and sediment thickness. *Ocean Modell.*, **32**, 36-43 (2010).

[17] Holmes, M. Generating samples of an internal wave field constrained by the Garett-Munk spectrum. Unpublished (2007) .

[18] Hida, T., Hitsuda, M. *Gaussian Processes*. American Mathematical Society (1990).

[19] `http://en.wikipedia.org/wiki/TOPEX/Poseidon` (visited on 23 July 2014).

[20] Egbert, G. D., & Erofeeva, S. Y. Efficient inverse modeling of barotropic ocean tides, *J. Atmos. Oceanic Technol.*, **19(2)**, 183-204 (2002).

[21] Gouretski, V. V., & Koltermann, K. P. WOCE Global Hydrographic Climatology. *A Technical Report*, **35** (2004) and `http://www.nodc.noaa.gov/woce/wdiu/` (visited on 23 July 2014).

[22] McDougall, T. J. & Barker P. M. *Getting started with TEOS-10 and the Gibbs Seawater (GSW) Oceanographic Toolbox*, 28pp., SCOR/IAPSO WG127, ISBN 978-0-646-55621-5 (2011).

[23] Sutherland, B. *Propagation, Stability and Instability of Small Amplitude Internal Waves*. Lecture notes, University of Alberta (2013).

[24] Munday, D. R., Allison, L. C., Johnson, H. L. & Marshall, D. P. Remote forcing of the Antarctic Circumpolar Current by diapycnal mixing. *Geophys. Res. Lett.* **38** (2011)

[25] St. Laurent, L. C., Simmons, H. L. & Jayne, S. R. Estimating tidally driven mixing in the deep ocean. *Geophys. Res. Lett.* **29** (2002)

[26] Polzin, K. L. A heuristic description of internal wave dynamics. *J. Phys. Oceanogr.* **34** (2004)

[27] Melet, A., Hallberg, R., Legg, S. & Polzin, K. Sensitivity of the ocean state to the vertical distribution of internal-tide-driven mixing. *J. Phys. Oceanogr.* **43**, 602-615 (2013)

[28] Melet, A. et al. Internal tide generation by abyssal hills using analytical theory. *J. Geophys. Res.* **118**, 6303-6318 (2013).

[29] Jayne, S. R. The impact of abyssal mixing parametrization in an ocean general circulation model. *J. Phys. Oceanogr.* **39**, 1756-1775 (2009).

[30] Talley, L. D. Closure of the global overturning circulation through the Indian, Pacific and Southern Oceans. *Oceanography* **26** (2013).

[31] Overturning circulation driven by breaking internal waves in the deep ocean. *Geophys. Res. Lett.*, **40**, 3133-3137 (2013).

[32] Gill, A. E. *Atmosphere-Ocean Dynamics* (Academic Press, London, 2006).

[33] Whalen, C. B., Talley, L. D. & MacKinnon, J. A. Spatial and temporal variability of global ocean mixing inferred from Argo profiles. *Geophys. Res. Lett.* **39**, L18612 (2012)

[34] Klymak, J. M. et al. An estimate of tidal energy lost to turbulence at the Hawaiian ridge. *J. Phys. Oceanogr.* **36**, 1148-1164 (2006).

[35] Alford, M. H. et al. Energy flux and dissipation in Luzon Strait: two tales of two ridges. *J. Phys. Oceanogr.* **41**, 2211-2222 (2011).

[36] Staquet, C. & Sommeria, J. Internal gravity waves: From instabilities to turbulence. *Ann. Rev. Fluid Mech.*, **34**, 559-93 (2002).

[37] Nikurashin, M. & Legg, S. A mechanism for local dissipation of internal tides generated at rough bathymetry *J. Phys. Oceanogr.*, **41**, 378-395 (2010).